



# A Catalog of Periodic Variables in Open Clusters M35 and NGC 2158

M. Soares-Furtado<sup>1,3</sup>, J. D. Hartman<sup>1</sup>, W. Bhatti<sup>1</sup>, L. G. Bouma<sup>1</sup>, T. Barna<sup>2</sup>, and G. Á. Bakos<sup>1,4,5</sup>

<sup>1</sup>Department of Astrophysical Sciences, Princeton University, Princeton, NJ 08544, USA; [msoares@princeton.edu](mailto:msoares@princeton.edu)

<sup>2</sup>Department of Physics & Astronomy, Rutgers University, 136 Frelinghuysen Rd., Piscataway, NJ 08854, USA

Received 2019 February 24; revised 2019 November 17; accepted 2019 November 20; published 2020 January 16

## Abstract

We present a catalog of 1143 periodic variables, compiled from our image-subtracted photometric analysis of the *K2* Campaign-0 super stamp. This super stamp is centered on the open clusters M35 and NGC 2158. Approximately 46% of our periodic variables were previously unreported. Of the catalog variables, we find that 331 are members of M35 and 56 are members of NGC 2158 ( $P_m > 0.5$ ). Our catalog contains two new transiting exoplanet candidates, both of which orbit field stars. The smaller planet candidate has a radius of  $0.35 \pm 0.04 R_J$  and orbits a K dwarf ( $K_p = 15.4$  mag) with a transit depth of 2.9 millimag. The larger planet candidate has a radius of  $0.72 \pm 0.02 R_J$  and orbits a late G-type star ( $K_p = 15.7$  mag) with a transit depth of 2.2 millimag. The larger planet candidate may be an unresolved binary or a false alarm. Our catalog includes 44 eclipsing binaries (EBs), including ten new detections. Of the EBs, one is an M35 member and five are NGC 2158 members. Our catalog contains a total of 1097 nontransiting variable stars, including a field  $\delta$  Cepheid exhibiting double mode pulsations, 561 rotational variables, and 251 pulsating variables (primarily  $\gamma$  Doradus and  $\delta$  Scuti types). The periods of our catalog sources range between 43 minutes to 24 days. The known ages of our reported cluster variables will facilitate investigations of a variety of stellar evolutionary processes.

*Unified Astronomy Thesaurus concepts:* [Transit photometry \(1709\)](#)

*Supporting material:* machine-readable table

## 1. Introduction

In 2017, we released 3960 light curves (Soares-Furtado et al. 2017) for stars of  $9.7 \text{ mag} < V < 18.7 \text{ mag}$  in the *K2* Campaign-0 (hereafter K2C0) super stamp. The super stamp is centered on the open clusters Messier 35 (NGC 2168, hereafter M35) and NGC 2158. We obtained high-precision photometry with reduced blending by developing an image subtraction pipeline tailored to address the *K2*-specific mission systematics. With only two operating gyroscopic reaction wheels, the *K2* systematics are dominated by the low-frequency motion that is induced by solar pressure and the subsequent thruster firings that are intended to correct for the drift of the spacecraft. Sources drift across two to three pixels throughout each cycle. Our *K2* image subtraction pipeline methodology is discussed in depth by Huang et al. (2015).

Image subtraction facilitates the analysis of time-series data in densely populated regions, such as crowded stellar cluster fields, particularly in regions near the cluster cores. Our light curves were corrected using the Trend Filtering Algorithm (TFA) outlined by Kovács et al. (2005). When compared with other methods used to examine this same data set, our TFA-corrected light curves were found to have marginally higher photometric precision across all the timescales investigated. The K2C0 light curves are hosted at <http://k2.hatsurveys.org/archive/>. In addition to the K2C0 analysis, this method has been extended to analyze other *K2* regions. Huang et al. (2015) performed an analysis of nearly 23,000 sources in the *K2* Campaign-1 field. It has been used to extract high-precision microlensing signals near the Galactic bulge from the *K2* Campaign-9 data set (Zhu et al. 2017a, 2017b). The method has also been applied to the globular

cluster M4, resulting in the detection of a new variable class known as the millimagnitude RR Lyrae (Wallace et al. 2019b, 2019a).

Despite the challenges due to crowding, variability searches in cluster fields have led to some important discoveries. Much of the recent success was made possible by the cluster time-series data provided by the *Kepler* and *K2* transit surveys. Among the clusters observed are the Hyades, the Pleiades, M4, M18, M21, M25, M35, M44 (Praesepe), M45, M67, M80, NGC 1647, NGC 2158, NGC 6717, NGC 6774 (Ruprecht 147), NGC 6791, NGC 6811, NGC 6819, and NGC 6866. To date, the transit search technique has revealed  $\sim 10$  confirmed exoplanets orbiting stars in open clusters (David 2018, and references therein). The first exoplanet detected in an open cluster by the transit method was found using *Kepler* data less than six years ago (Meibom et al. 2013). The majority of cluster exoplanet candidates have been revealed by the *K2* survey (Ciardi et al. 2018, and references therein). A census analysis of exoplanets found in stellar clusters may shed light on the underlying physical processes driving planetary formation and evolution, particularly since these systems span a wide age and metallicity range. Determining the planet occurrence rates and planet architectures within clusters would have far-reaching significance, as all stars—and therefore all planetary systems—likely form in clustered environments (e.g., Portegies Zwart et al. 2010). To paint a complete picture of the pertinent physical mechanisms at play, more cluster planet detections are required, as the majority have been found among Sun-like stars in the highly irradiated regime.

There is also value in the detection and characterization of eclipsing binaries (EBs) in stellar clusters. Having precise radii measurements of evolved EBs provides a useful age estimate for stellar clusters, offering tight constraints on both the distance and reddening of cluster members. Sandquist et al. (2013) demonstrated this technique by using *Kepler* observations of the EB system WOCs 23009 to constrain the age of NGC 6819. This

<sup>3</sup> National Science Foundation Graduate Research Fellow.

<sup>4</sup> Packard Fellow.

<sup>5</sup> Alfred P. Sloan Research Fellow.

resulted in an age estimate of  $2.62 \pm 0.25$  Gyr with stellar model physics responsible for systematic uncertainties at the level of 10%. This age estimate was further constrained to unprecedented precision when the number of detected EBs in the system substantially increased (Brewer et al. 2016).

M35 is a compelling region to search for periodic variability, as the stellar constituents provide a significant contribution to the high-mass end of the initial–final mass relation (IFMR; Williams et al. 2009). These stars are important probes for our models of stellar evolution. They represent the lower mass limit for the transition between the class of stars that will evolve to produce white dwarfs and those that will end their lives as violent supernovae. Detecting EBs in M35 not only has the potential to enhance the precision of the high-mass end of the IFMR for white dwarfs, it may also reduce uncertainties in the masses of progenitor stars within the white dwarf–neutron star transition. Section 8 describes the cluster-affiliated EBs in our data set.

Detections of Cepheids and RR Lyrae stars are also important, as these sources map the substructures and stellar populations of the Milky Way. Over the course of its mission, Kepler observations significantly increased the number of Cepheid and RR Lyrae detections, bringing the counts into the hundreds and thousands, respectively (Molnár et al. 2018). While Cepheid variables are less common than RR Lyrae stars, their greater luminosity makes them easier to detect. This often permits their detection in regions where blending has not been mitigated. RR Lyrae stars, in contrast, often require blending mitigation techniques to be detected.

Stellar rotation rates can be obtained from the time series analysis of photometric variations produced by rotating starspots (e.g., Irwin & Bouvier 2009). Rotational variables found in stellar clusters are particularly important probes to test stellar evolutionary models. The field of gyrochronology was built upon the work of Skumanich (1972), whereby the projected stellar rotational velocities ( $v \sin i$ ) among stars within the Hyades and Pleiades clusters were shown to decrease as the square root of the star’s age. For some main-sequence (MS) stars, gyrochronology is the most precise chronometer available (e.g., Epstein & Pinsonneault 2014). The rotation periods of late MS stars are also dependent upon mass (e.g., Barnes 2007; Irwin & Bouvier 2009; Meibom et al. 2009, 2011, 2015), and much work has been done to model the empirical relations between these stellar parameters (e.g., Kawaler 1989; Barnes 2003, 2007, 2010; Mamajek & Hillenbrand 2008; Angus et al. 2015), as well as to probe the underlying physical processes driving these relations (e.g., Reiners & Mohanty 2012; Gallet & Bouvier 2013). Young coeval MS stellar populations have been shown to display rotation rates that range by two orders of magnitude (e.g., Irwin et al. 2008; Irwin & Bouvier 2009; Hartman et al. 2010). As a cluster ages, the stellar rotation rates quickly converge (e.g., Hartman et al. 2009; Meibom et al. 2011). It has been proposed that the mechanism driving this convergence is the loss of angular momentum via stellar winds (Weber & Davis 1967), but there are still many uncertainties associated with the corresponding models. To effectively probe theoretical models of angular momentum evolution stellar rotation rates must be observed across a wide range of stellar ages and masses.

To contribute to these efforts, we used data from the *K2* transit survey to search open cluster systems for the presence of planets, EBs, rotational variables, and pulsational variables. In this paper, we present the results of a periodic variability search performed on the sources in the K2C0 super stamp. We assign cluster

membership probabilities to our identified variables, compare our sources to the results from prior searches conducted in this field, discuss the newly identified variables, and make our results publicly available. Section 2 provides some background information for the K2C0 open clusters. The K2C0 photometric observations are described in Section 2.3. Section 3 describes the technical steps involved in our assimilation of the periodic variable catalog. Section 4 summarizes the contents of our variable catalog. That section includes relevant catalog census information, such as the distributions of stellar type, variable class, and cluster membership. We also discuss the period–magnitude relation obtained for M35 rotational variables. Section 5 compares our variable catalog results to the results generated by prior searches conducted within this field. Section 6 describes the new variables that were found in our search. In Section 7, we review our candidate transiting exoplanet detections. We discuss our EB detections in Section 8. In Section 9, we discuss our analysis of the double-mode  $\delta$  Cepheid variable, V0371 Gem. In Section 10, we provide example light curves for a subset of rotational variables,  $\gamma$  Doradus variables, and  $\delta$  Scuti variables. In Section 11, we summarize our findings.

## 2. The K2C0 Open Clusters and Data

### 2.1. M35

With an age of  $\sim 150$  Myr (Meibom et al. 2009), M35 is a critical system to probe for exoplanets, as planets undergo rapid evolutionary changes during the first few hundred million years after formation (Adams & Laughlin 2006). Such a cluster is a useful system to test theories of planetary formation and planet migration timescales. The angular diameter of the cluster is  $0.5^\circ$  and the stars are well-dispersed relative to other open clusters. This reduces source confusion and permits multiobject spectroscopy follow-up. Crowding is a concern near the core of the cluster. Cantat-Gaudin et al. (2018, hereafter CG18) used *Gaia* DR2 data to infer a distance of 861 pc to the cluster. The inferred reddening for this system is estimated to be  $E(B-V) = 0.255 \pm 0.024$  mag (Sung & Bessell 1999).

The stars comprising the M35 MS span  $\sim 14$  magnitudes in brightness in the  $V$  versus  $B-V$  plane. The hottest M35 members are classified as B3 in spectral type (Kalirai et al. 2003). Using the overshooting models of Girardi et al. (2000), the cluster main sequence turn-off (MSTO) mass has been estimated as  $\sim 3.75 M_\odot$ . This indicates an age that is similar to that of the Pleiades (M35 is  $\sim 150$  Myr and the Pleiades is  $\sim 125$  Myr; Vidal 1973). In contrast to the Pleiades, however, M35 is rather metal-poor, with a metallicity of  $[\text{Fe}/\text{H}] = -0.21 \pm 0.10$  (Barrado y Navascués et al. 2001).

The median proper motion of the cluster is measured as  $(\mu_\alpha \cos \delta, \mu_\delta) = (2.308, -2.905) \pm (0.239, 0.235)$  mas yr $^{-1}$  (Cantat-Gaudin et al. 2018). Due to this low proper motion, as well as a low Galactic latitude, there has been much disagreement regarding the number of cluster members. Early estimates determined  $\sim 500$  stellar members (Cudworth 1971). A counting analysis of MS members performed 30 yr later found  $\sim 1700$  cluster members (Barrado y Navascués et al. 2001). The most recent estimate, determined by CG18, found 1325 stellar members ( $P_m > 0.5$ ). Unfortunately, this study did not include the most radially distant members within the cluster (as measured by the 2D projected distance from the cluster core). In an effort to ensure completeness in our M35 membership analysis, we

employed results from multiple membership catalogs. These catalogs are described in Section 3.4.

## 2.2. NGC 2158

Separated from M35 by  $25'$ , the angular diameter of NGC 2158 is  $5'$ . Severe blending is a concern for this densely packed cluster, which lies at a distance of 4.5 kpc (Cantat-Gaudin et al. 2018). The system was considered to be a globular cluster until Shapley (1930) carefully investigated individual sources. With an age estimate of 2 Gyr, NGC 2158 is too young to be classified as a globular cluster (Carraro et al. 2002) and has been deemed a member of the old thin disk population (Jacobson et al. 2009). The age is old enough for the open cluster to have undergone mass segregation.

The light from the cluster is dominated by an underlying population of yellow stars with the hottest members classified as F0 in spectral type. The cluster MSTO mass is estimated at  $\sim 1.3 M_{\odot}$ , which was determined using the cluster age and a  $Z = 0.0048$  isochrone (Carraro et al. 2002). Although NGC 2158 is much older than M35, it is richer in metals ( $[\text{Fe}/\text{H}] = -0.03 \pm 0.14$ ). The inferred reddening for the cluster is estimated at  $E(B-V) = 0.55 \pm 0.10$  mag (Carraro et al. 2002).

Cantat-Gaudin et al. (2018) estimated a cluster proper motion of  $(\mu_{\alpha} \cos \delta, \mu_{\delta}) = (-0.177, -2.002) \pm (0.185, 0.173)$  mas yr $^{-1}$ . While NGC 2158 is one of the most populous open clusters, its low proper motion poses a formidable challenge to cluster membership analysis. In an effort to ensure completeness in our cluster membership analysis, we employed multiple membership catalogs. These catalogs were produced using proper motions as well as multiwavelength photometry (optical and near-infrared). Given the spheroidal shape of this cluster, we incorporated a King model fit to weight the associated membership probabilities. Our cluster membership analysis is described further in Section 3.4.

## 2.3. The K2C0 Data Set and Processing

The full K2 field of view (FOV) is 115 square degrees and comprises an angular diameter of six degrees on the sky. The FOV is produced by the combination of 21 CCD modules, each of which is composed of two  $2200 \times 1024$  pixel CCDs. The entirety of the K2C0 super stamp lies on a single module. The K2C0 super stamp is an aggregate of 154 postage stamp images that are toggled across a field centered on the open clusters M35 and NGC 2158. The super stamp is  $0.5^{\circ}$  in angular diameter (about the size of M35). Each postage stamp is  $50 \times 50$  pixels in size. Both the presence of the open clusters and the proximity to the dense Galactic anticenter results in significant crowding.

The K2C0 field was observed from 2014 March to May. The telescope was mistakenly placed in coarse-pointing tracking mode during the first half of the campaign. Our analysis of the K2C0 super stamp solely employed cadences captured when the instrument tracking was set to the fine-pointing mode, which reduced our total number of cadences to 1551 (beginning with long cadence number 89347). Each cadence observation consists of a 29 minute integrated exposure, and these data span an observation window of 31 days. The K2 survey never returned to this same field in subsequent campaigns. We examined stars in the K2C0 field as faint as  $V = 18.7$  mag, corresponding to a *Kepler* magnitude of  $K_p = 16$  mag. To perform source extraction, we utilized The Fourth U.S. Naval Observatory CCD Astrograph

Catalog (UCAC4) and The Ecliptic Plane Input Catalog. UCAC4 is supplemented by the Two Micron All-Sky Survey (2MASS), which provides photometric data for 110 million stars and the AAVSO Photometric All-Sky Survey, which provides photometric data for over 50 million stars. We applied an image subtraction process to the data, using the technique outlined by Alard & Lupton (1998) and Alard (2000).

This process is summarized by the following sequence of steps:

1. For each cadence, the target pixel frames from our module of interest are assembled into a super stamp.
2. For each super stamp cadence, we perform source extraction using the UCAC4 star catalog. We determine the astrometric transformation between UCAC4 sources and the extracted K2 sources.
3. A sharp super stamp image with median directional pointing is selected. We call this the “astrometric reference frame.”
4. All cadences are spatially transformed to a common coordinate frame. This step minimizes spacecraft drift and allows for a more accurate model of the instrument’s motion in our detrending procedure.
5. A stacked median average of all the translated K2C0 frames are generated. We call this the “master photometric reference frame.”
6. Each cadence is subtracted from the master photometric reference frame, resulting in a variable field with reduced blending.
7. Photometry is performed on the sources in each image-subtracted cadence.
8. The light curves are assembled for all sources.
9. A high-pass filter with one-day binning is applied to the data. The decorrelation procedure modeled by Vanderburg & Johnson (2014) is applied.
10. The TFA correction as outlined by Kovács et al. (2005) is applied to remove further systematics.

Our data reduction procedure is described in more detail in Huang et al. (2015), and the detrending procedure is described in more detail in Soares-Furtado et al. (2017).

## 3. From K2C0 Light Curves to Catalog Variables

From our initial set of 3960 image-subtracted K2C0 sources, 1143 were identified as periodic variables and have been added to our catalog. A digital version of the catalog has been made publicly available, and is hosted online in a flexible format at <https://k2.hatsurveys.org/archive/>. The sources excluded from our catalog were either found not to vary periodically within our investigated period bounds (0.03–31 days) or were identified as secondary blends. We describe our procedure for identifying the primary variable source within a blended group in Section 3.2.

### 3.1. Periodogram Searches

To detect periodic variables within our nonuniformly sampled, image-subtracted photometry, we employed three distinct periodogram searches. In our search for transit candidates, which includes detached stellar EB systems and transiting exoplanets, we used the Box-fitting Least Squares (BLS) transit search routine (Kovács et al. 2002). To detect and classify variability that is more



sinusoidal in character, we used the generalized Lomb–Scargle (LS) algorithm (Scargle 1982; Zechmeister & Kürster 2009) and the phase dispersion minimization (PDM) algorithm (Stellingwerf 1978).

We ran period searches on our 3960 light curves (LCs) using the Python module *Astrobase* v0.2.2 (Bhatti et al. 2018) and the command line utility *VARTOOLS* (Hartman & Bakos 2016). The search results were reviewed both by eye and by implementing automated cut-off metrics, which are described in Sections 3.1.1–3.1.3. Two observers looked through the entire set, generating a culled subset of variables. When the variable classification or period designation was unclear, the LCs were flagged and reviewed by two additional observers. We include comments in the digital catalog to address ambiguous sources.

### 3.1.1. BLS Periodogram Parameters

Using *VARTOOLS*, we employed the BLS algorithm search on our time-series data to reveal LC sources with periodic “box”-shaped features. The algorithm relied on two variables: (1) the span of the observation window for a given source, and (2) the mean density estimate of the target star—which is directly related to observable parameters. The span of the observation window was generally  $T_{\text{span}} = 31$  days, but a subset of sources near the edges of the super stamp were sampled over shorter intervals. The stellar mean density was determined using the star’s  $V$ – $K$  color with the assumption that the source was a zero-age MS star with a metallicity of  $[\text{Fe}/\text{H}] = 0.0$ . Using density estimates, we performed a bilinear interpolation of the tabulated stellar isochrone models generated by Yi et al. (2001).

The minimum period threshold was set to  $a/R_\star > 1$ , where  $a/R_\star$  is the ratio of the orbital separation to the size of the stellar radius. Recalling the relation

$$\frac{a}{R_\star} = \left( \frac{GT^2\rho}{3\pi} \right)^{\frac{1}{3}} > 1, \quad (1)$$

we set a minimum search period of

$$T_{\text{min}} = \sqrt{3\pi/(\rho G)}, \quad (2)$$

where  $G$  is the gravitational constant and  $\rho$  is the mean density of the host star. This relation relies on the assumption that the mass of the transiting object is negligible when compared to the mass of the host star.

To determine the number of phase bins needed, we computed  $q$ , the transit duration in units of phase for circular, edge-on orbits. The stellar density is used in this implementation of the BLS search to determine the range of transit duration values to search at a given period. The minimum transit duration in phase at the longest period,  $q_{\text{min}}$ , is equal to  $1/2q$ . This can be represented as

$$q_{\text{min}} = 0.5q = 0.5 \left( \pi \frac{a}{R_\star} \right)^{-1}. \quad (3)$$

The number of bins,  $n_{\text{bin}}$ , is calculated as

$$n_{\text{bin}} = \frac{2}{q_{\text{min}}} = \left( \frac{64\pi^2 G \rho T_{\text{span}}}{3} \right)^{1/3}, \quad (4)$$

and the frequency step size is given by the relation

$$\Delta f = \frac{0.25}{(T_{\text{span}})(q_{\text{min}})}. \quad (5)$$

For reference, some typical numbers for these parameters are  $n_{\text{bin}} = 850$  and  $\Delta f = 2 \times 10^{-10} \text{ s}^{-1}$ . As a careful secondary check, we repeated our BLS search using the *Astrobase* platform. For the BLS search, we imposed a frequency range of  $1/T_{\text{span}} - 1/T_{\text{min}}$ , where  $T_{\text{min}}$  is the cadence integration time. We used a uniform frequency step size of  $\Delta f = 8.0 \times 10^{-5} \text{ s}^{-1}$ , and fixed minimum and maximum in-phase transit durations of  $q_{\text{min}} = 0.01$  and  $q_{\text{max}} = 0.8$ .

All BLS results were reviewed by eye for characteristic box-shaped dimming (constant in depth and flat-bottomed). The period, phase, and transit durations were inspected. We also checked LCs for the presence of a secondary eclipse that would be indicative of an EB. To find contact binaries, the corresponding LS and PDM periodograms were checked for the characteristic arc-shaped LC signature that is indicative of W Ursae Majoris variables (low-mass contact binaries). We employed a signal-to-noise metric,  $S/N_{\text{pink}}$ , measured using *VARTOOLS* and defined by Pont et al. (2006) as

$$S/N_{\text{pink}} = \sqrt{\frac{\delta_m^2}{(\sigma_w^2/n_t) + (\sigma_r^2/N_t)}}, \quad (6)$$

where  $n_t$  is the number of data points present in the transit and  $N_t$  is the number of transits sampled. The transit depth is given by  $\delta m$ , which provides a proxy of the signal. The red noise of the light curve is represented by  $\sigma_r$ . This is calculated after subtracting the transit model, binning residuals in time with bins equal in size to the transit duration, and then taking the standard deviation. The variable  $\sigma_w$  represents the root mean square (rms) scatter of the unbinned LC after subtracting the transit model (generally referred to as the “white noise”). Instead of imposing a firm cut-off for the  $S/N_{\text{pink}}$  metric, which would eliminate real transiting sources with highly correlated noise and outliers, we use the threshold  $S/N_{\text{pink}} < 17$  as a flag for a more in-depth investigation. The catalog variables with low  $S/N_{\text{pink}}$  metrics were deemed as compelling variable sources, despite this low metric, after an inspection of the LC by eye. For reference,  $S/N_{\text{pink}} = 36$  is the median value among transiting sources in our catalog.

### 3.1.2. LS Periodogram Parameters

To unveil rotating and pulsating variable stars in the K2C0 LC sample, we executed a generalized Lomb–Scargle (LS) periodogram search (Zechmeister & Kürster 2009) with *VARTOOLS*. This search identified the five highest amplitude peaks in the power spectrum. We applied a fixed frequency range of  $3.85 \times 10^{-7}$  to  $3.85 \times 10^{-4} \text{ s}^{-1}$  and a uniform frequency step size of

$$\Delta f = \frac{sb}{T_{\text{span}}} = 3.73 \times 10^{-9} \text{ s}^{-1}. \quad (7)$$

The variable  $sb$  represents the subsample, which was set to  $sb = 0.01$ . The observation time window was set to  $T_{\text{span}} = 31$  days. We also calculated the formal false alarm probability (FAP) derived with *VARTOOLS*,  $\log(\text{FAP})$ , as well as the



signal-to-noise ratio (S/N) for each of the identified peaks, S/N. Our threshold was set to  $S/N > 7$ , where S/N is given by the equation

$$S/N = \frac{LS - \overline{LS}}{\sigma_{LS}}, \quad (8)$$

where

$$LS = \frac{\chi_0^2 - \chi(f)^2}{\chi_0^2}. \quad (9)$$

Here,  $\chi_0^2$  is the value of  $\chi^2$  about the weighted mean and  $\chi(f)^2$  is the value of  $\chi^2$  about the best-fit sinusoidal signal with frequency  $f$ . All the identified peak periods are whitened and the periodograms are then recomputed before searching for subsequent peak periods. Sources with high log(FAP) values were flagged as suspicious and carefully investigated by eye. Only four catalog sources have a  $\log(\text{FAP}) > 1$ , making up less than 0.4% of our catalog. For comparison, we used *Astrobase* to perform a generalized LS periodogram search on all LCs, using a frequency range of  $1/T_{\text{span}} - 1/T_{\text{min}}$  and the *Astrobase* default uniform frequency step size of  $\Delta f = 1.0 \times 10^{-4} \text{ s}^{-1}$ .

### 3.1.3. PDM Periodogram Parameters

Using *Astrobase*, we performed a PDM periodogram search with a frequency range  $1/T_{\text{span}} - 1/T_{\text{min}}$  and a uniform frequency step size of  $\Delta f = 1.0 \times 10^{-4} \text{ s}^{-1}$ . The results of the LS and PDM periodograms were carefully compared by eye to discern the most accurate period for each target. The best selected period is listed in *Column 6 (P)* of our variable catalog.

### 3.2. Identifying Primary Variables in Blended Groups

After the identification of periodic sources in the K2C0 super stamp, we sought to mitigate any degeneracies in variability—these are commonly referred to as *blends*. To identify whether a given target source is blended, we compare the top five periods identified by the power spectrum, as well as the associated harmonics, to those corresponding to the neighboring sources within a 10 pixel radius (equivalent to  $40''$ ). Some stars contained as many as 50 blended neighbors. If no blends were found at this initial step, the target was identified as a conclusive primary. The optimal method to distinguish a primary source within a blended group is dependent upon the variable classification of a given source. As a first step, we distinguished by eye whether the target LC either (a) displayed the characteristic box-shaped dimming indicative of a transit event or (b) displayed sinusoidal variations indicative of a pulsating, rotating, or erupting variable.

To distinguish a primary source among the candidate EBs and transiting exoplanets, we compared the transit depth, transit duration, and the  $S/N_{\text{pink}}$  measurement among the members of a blended group. Primary sources were designated as those with the following characteristics: (a) the deepest transit depth among sources in the blended group, (b) a sensible transit duration (given the corresponding color information), and (c) the strongest  $S/N_{\text{pink}}$  among sources in the blended group. While the third criterion was generally true for our designated blended primaries, this was the least significant criterion in our selection process.

To identify the primary source in a set of pulsating and rotating variables, we fit an order-3 Fourier series to the differential flux time series for each of the five periods identified in the peak power spectrum. This fit was performed on all sources within the blended group. We then compared the corresponding Fourier fit amplitudes. Primary sources were designated as those with the largest Fourier fit amplitude. If the amplitude difference between the target and any member of the blended group was  $< 0.4$  millimag, the target was labeled as an ambiguous blend. We list the blend status for identified variables in *Column 10 (Blend)* of our catalog. The distribution of identified primaries and ambiguous blends is discussed in Section 4.1.

### 3.3. Periodic Variable Source Classification

The 1143 periodic variables in our culled catalog were initially separated into two distinct groups: (1) those displaying box-like dips in their LCs (indicative of an EB or exoplanet transit candidate) and (2) those with sinusoidal LC signatures indicative of rotating or pulsating variables.

Sources classified as transiting exoplanet candidates are those with transit depths, transit durations, and orbital separations that are consistent with a star–planet system. To mitigate false positives among the transiting exoplanet candidates, we incorporated spectroscopic measurements, *Gaia* parallaxes, stellar density estimates, and relevant cluster parameters (such as age and metallicity). Sources classified as candidate transiting exoplanets were labeled with the class identifier *Transit*, also found in *Column 8 (Class)* in our catalog. We discuss our exoplanet candidate sources in Section 7.

To distinguish an EB from an exoplanet transit candidate, we searched for signatures of a secondary eclipse among the phase-folded LCs. This secondary eclipse is reminiscent of an EB system, as transiting exoplanet candidates do not exhibit two distinct minima. Also added to the EB class were sources with characteristic arc-shaped LC signatures indicative of W Ursae Majoris variables (low-mass contact binaries). Sources classified as EBs were labeled with the class identifier *EB* in *Column 8 (Class)* of our variable catalog. We discuss our EB sources in Section 8.

Non-transiting variable sources were examined for characteristic LC signatures produced from stellar pulsations, rotation, and/or eruptions. Sources were classified using the following parameters: (a) the source period, (b) the shape of the LC, (c) the photometric variability amplitude as measured from the Fourier series fit to the differential magnitude (as described in Section 3.2, except that we used a Fourier fit on the magnitude rather than the flux), and (e) the *Gaia* DR2 derived parameters of temperature, radius, and luminosity. The reddened-corrected  $J - K$  difference values were not used in our classification given the high associated uncertainties. All the sources designated as rotational variables were checked to ensure that (a) the corresponding rotational velocities did not exceed the stellar break-up speed and (b) the effective temperature does not exceed the expected temperature ceiling of  $T_{\text{eff}} = 6250 \text{ K}$ , above which surface magnetic activity is unexpected among dwarf stars. Sources that violate these conditions are inspected for reclassification and designated as *Misc* if a distinct class cannot be identified. In *Column 6 (P)* of our variable catalog, we list the source periods used for variable classification. Most often, this period corresponds to the frequency responsible for the peak maximum in the LS power

spectrum. There are cases where the PDM identified period was selected or lower amplitude peaks were determined to be responsible for the photometric variations. The *Column 71 (Comment)* of our variable catalog indicates when a period other than the LS power spectrum peak maximum was selected.

We created a variable classification pipeline using the relevant classes listed in the AAVSO International Variable Star Index (VSX; Watson et al. 2006, 2017) and in Karttunen et al. (2017). Given our sample period and  $\Delta\text{mag}$  bounds, our classification pipeline searched for nondescript rotational variables and pulsators of the following types:  $\delta$  Scuti (also known as dwarf Cepheids), RR Lyrae,  $\gamma$  Doradus, Cepheids,  $\beta$  Cepheids, and slowly pulsating B-type variables. Some of these classes were omitted entirely, as they were outside the period bounds of our sample, such as rapidly oscillating Ap stars and Mira variables. The pipeline procedure is outlined below.

1. We begin with the assumption that all the listed periodic variable classes within our period and  $\Delta\text{mag}$  amplitude bounds are possible for a given target star. These periodic variable classes are taken from the VSX, as they were listed in 2015, and from the classes listed in Table 14.1 of Karttunen et al. (2017).
2. We rule out variable classes in a sequence of steps. In our first elimination round, we compare the amplitude calculated from the Fourier series fit to the differential magnitude to the  $\Delta\text{mag}$  bounds corresponding to each of the potential variable classes. At this step, classes that do not encompass the target amplitude are eliminated. The rotating class cannot be eliminated at this step given its wide range of brightness variations.
3. We then determine if the period of the target is compatible with the period bounds for each of the remaining variable class categories. Classes that do not include the designated source period are eliminated at this step.
4. We employ the associated *Gaia*-derived luminosity and temperature (and the corresponding errors) to determine if further classes may be ruled out. Source temperatures are used to see if the target is outside the instability strip ( $\pm \log_{10} T_{\text{eff}} = 0.5$  K), which would rule out pulsational variability.
5. The source is labeled as *Misc* if either all the classification categories have been eliminated or if multiple, indistinguishable classifications subsist.
6. We then compare our classification designations to those of pre-existing variable catalogs.

More massive stars ( $M_* > 2 M_{\odot}$ ) evolving off the MS will cross the instability strip at higher luminosities in the HR Diagram. The high mass and luminosity of these stars result in longer periods than the average  $\delta$  Scuti star, which can reach up to 1 day (e.g., Buchler & Szabó 2007; Buchler 2008; Smolec & Moskalik 2010). This is taken into consideration when we review the classification designation of a source.

Two blended sources that share a common periodic signature do not necessarily share the same variable classification. This is because there may be differences in their corresponding stellar classification. The results of our variable classification procedure are discussed in Section 4.2.

**Table 1**  
The Cluster Membership Probability Catalogs Used in Our Membership Analysis of M35 and NGC 2158

Cluster Membership		
Probability Catalogs		
M35		
Catalog	$N_{\text{cat}}$	$N_{\text{m,LC}}$
CG18	1,705	358
DANCe	338,392	1120
K13	100,801	1,084
NGC 2158		
Catalog	$N_{\text{cat}}$	$N_{\text{m,LC}}$
CG18	1,633	51
K13	20,640	752
D06	330	72

**Note.** The total number of sources in each catalog is given by  $N_{\text{cat}}$ . The total number of matches found when comparing our variables to those listed in the catalogs is given by  $N_{\text{m,LC}}$ . The catalogs are listed in descending order of precedence.

### 3.4. Determining Cluster Membership

#### 3.4.1. M35 Membership

To determine M35 cluster membership probabilities for as many of our catalog variables as possible, it was necessary to employ multiple cluster membership catalogs. The cluster membership catalogs and the matching procedures are outlined in Sections 3.4.3–3.4.6. In order of precedence, the catalogs employed included (1) the CG18 *Gaia* DR2 membership catalog, (2) the Bouy et al. (2015) multi-epoch DANCe catalog (hereafter DANCe), and (3) the Kharchenko et al. (2013) membership catalog (hereafter K13). If an M35 membership probability was not found in the CG18 *Gaia* DR2 catalog, we searched for a match in the DANCe catalog. If the source remained unmatched, we performed a final search through the K13 catalog. The CG18 membership probability catalog concentrated on more central regions of the cluster and excluded many sources in the DANCe catalog, which provided the bulk of our listed M35 membership probabilities. The K13 catalog provided M35 membership probabilities for four sources that were excluded from both the CG18 and DANCe catalogs. A total of 16 catalog sources remained unmatched after searching each of the three catalogs. In Table 1, we provide the size of each of the cluster membership catalogs, as well as the number of source matches found. The membership probabilities are listed in *Column 64 (PM35)* of the variable catalog.

#### 3.4.2. NGC 2158 Membership

We followed a similar approach to ascribe NGC 2158 membership probabilities. In order of precedence, the catalogs employed included (1) the CG18 *Gaia* DR2-derived catalog, which focused primarily on the more central regions of the cluster, (2) the aforementioned K13 catalog, and (3) the Dias et al. (2006) catalog (hereafter D06).<sup>6</sup> The K13 catalog supplied the vast majority of membership probabilities. We

<sup>6</sup> The DANCe catalog did not include NGC 2158 membership probabilities and is omitted from the procedure.

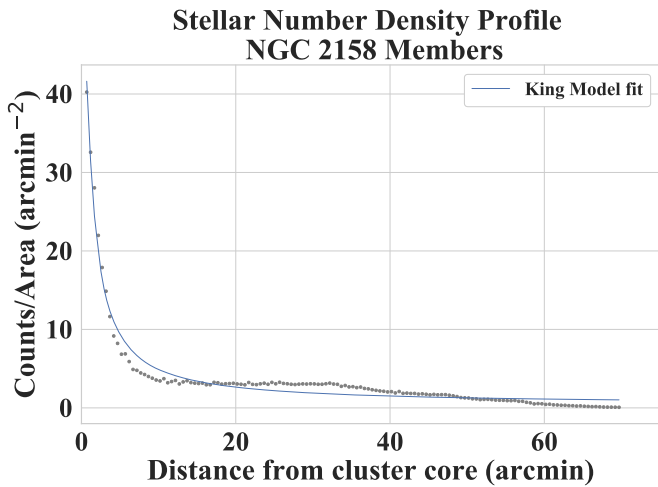


**Figure 1.** King model fit to  $\sim 97,000$  sources in the **CG18** *Gaia* DR2 data set, positioned about the core of NGC 2158. Our fit is shown in blue, which determined a core radius of  $r_c = 0.9'$  ( $\sim 1$  pc) and a tidal radius of  $r_t = 16'$  ( $\sim 21$  pc).

found 51 matches in the **CG18** catalog. The **D06** catalog provided membership probabilities for four sources excluded by the combined efforts of **CG18** and **K13**. One of these four sources, the rotating variable UCAC4-571-024298, is an NGC 2158 member. A total of 388 catalog sources remained unmatched after searching the three catalogs. In Table 1 we provide the size of each of the cluster membership catalogs, as well as the number of source matches found. The cluster membership catalogs and the matching procedures are outlined in Sections 3.4.3–3.4.6.

We found that many sources possessed high membership probabilities despite being positioned well outside the cluster tidal radius. Given the cluster’s low proper motion, similar to that of field stars, this was unsurprising. The spheroidal shape of the cluster permits a 2D King model fit to the spatial distribution of these sources (King 1962). To ensure a conservative membership likelihood for our sources, we weighted the catalog-derived membership probabilities by a King model fit. In the cases where a catalog match was not found, the King model weight was used as a membership proxy. The membership probabilities are listed in Column 65 (*PN2158*) of the variable catalog.

To calculate the membership probability derived by the King model ( $P_K$ ) for a given source, we used the method outlined in Li et al. (2018). The probability is given by  $P_K = (f_K - b)/(f_K)$ , where  $f_K$  is the King model fit to the stellar density profile and  $b$  is the background estimate. Our fit was performed on  $\sim 97,000$  *Gaia* DR2 sources out to a distance of  $70'$  from the cluster core. We employed the central coordinates measured by Cantat-Gaudin et al. (2018). Our fit is shown in Figure 1. From this fit, we estimate a core radius of  $r_c = 0.9'$  ( $\sim 1$  pc) and a tidal radius of  $r_t = 16'$  ( $\sim 21$  pc).

#### 3.4.3. *Gaia* DR2 Cluster Membership Catalog (CG18)

The **CG18** membership catalogs employed *Gaia* DR2 data to calculate cluster membership probabilities for stars in 1212 Milky Way stellar clusters (Cantat-Gaudin et al. 2018). Cluster membership probabilities were determined using the unsupervised membership assignment code, UPMASK, which performs

a k-means clustering analysis on the proper motions and parallaxes for a population of sources. The **CG18** M35 membership catalog contains a total of 1705 sources and the **CG18** NGC 2158 membership catalog contains 1633 sources. To find matches for our variable sources, we searched the membership catalog for sources with a separation  $< 5''$  and a *Gaia* magnitude difference of  $< 0.4$  mag. The *Gaia* magnitude difference is the difference between the reported DR2 *Gaia* magnitude and our calculated source *Gaia* magnitude using the *B*–*V* Johnson-Cousins algorithm described in Jordi et al. (2010). Among the two **CG18** cluster membership probability catalogs, we found a total of 409 source matches with 358 matches in the M35 catalog and 51 in the NGC 2158 catalog.

#### 3.4.4. The DANCe Cluster Membership Catalog

The DANCe cluster membership catalog was assembled using proper motion measurements and multi-wavelength (optical and near-infrared) photometry from some of the best ground-based archival data sets collected over the past 18 yr (Bouy et al. 2015). The team applied this method to two clusters, the Pleiades (Sarro et al. 2014) and M35 (Bouy et al. 2015). The M35 DANCe analysis resulted in significantly reduced membership probabilities for many sources that were considered cluster members in prior catalogs. Membership probabilities have not been provided for NGC 2158 by this group.

To identify cluster members, the team employed a training set, which was supplied by Barrado y Navascués et al. (2001) for M35. While Bouy et al. (2015) found that contamination from nearby NGC 2158 members did not reach more than  $\sim 2\%$ , they noted that it is a challenging system to analyze due to the cluster’s low proper motion and the overlap observed in the color–magnitude diagram (CMD) among cluster members and field sources. The DANCe catalog contains a total of 338,892 sources, 4349 of which have cluster membership probabilities of  $P_m > 0.5$ . Searching this catalog, we found a total of 1120 source matches, representing nearly our entire sample of K2C0 variables. This catalog provided membership probabilities for 772 sources unmatched in the **CG18** catalog. Similar to our approach of source matching in the **CG18** catalog, we searched for matches with a  $< 5''$  separation as well as a magnitude difference of  $< 0.4$  mag (*J* or *H*, depending on the data that was available for the target). We used this same source matching criteria for the **K13** and **D06** catalogs. These catalogs are described in Sections 3.4.5 and 3.4.6.

#### 3.4.5. The K13 Cluster Membership Catalog

The **K13** cluster membership catalog was part of the Milky Way Star Clusters project (Kharchenko et al. 2013), which resulted in the assignment of cluster membership probabilities for sources in 3006 Milky Way clusters. The results were obtained by employing kinematic and near-infrared photometric data from the all-sky PPMXL catalog (Roeser et al. 2010) and 2MASS (Curtis et al. 2013). The cluster membership probabilities were determined using the stellar source location with respect to the reference sequences, which include isochrones in photometric diagrams and/or the average cluster proper motion in kinematic diagrams. We found 1,084 sources with corresponding M35 membership probabilities, representing 95% of our variable catalog. This catalog provided M35



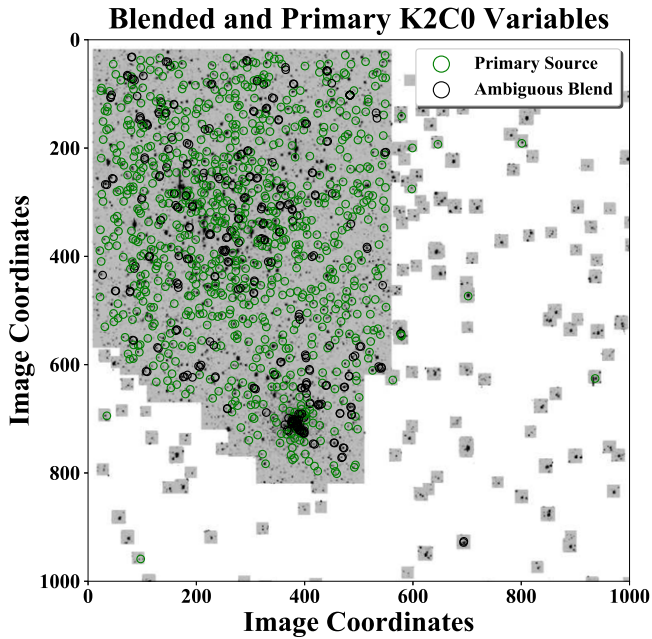


**Figure 2.** Two-dimensional projected spatial location of our identified primary variables (green circles) and ambiguously blended variables (gray circles). A collection of ambiguously blended variables is observed near the core of NGC 2158.

membership probabilities for four sources that were excluded from both the [CG18](#) and [DANCe](#) catalogs. We found 752 source matches with corresponding NGC 2158 membership probabilities. This catalog provided NGC 2158 membership probabilities for 708 sources that were excluded from the [CG18](#) catalog.

#### 3.4.6. The D06 Cluster Membership Catalogs

The [D06](#) cluster membership probability catalog is part of a cluster membership survey performed on 112 Milky Way open clusters, including M35 (Dias et al. 2001) and NGC 2158 (Dias et al. 2006). We used only the NGC 2158 cluster membership catalog, which was produced using positions and proper motions from the UCAC2 Catalog. To calculate the probability of cluster membership, the team employed a method proposed in Sanders (1971), which fits the relative proper motions to a maximum likelihood statistical model. We found a total of 72 source matches in the [D06](#) catalog for NGC 2158. This catalog provided NGC 2158 membership probabilities for four sources that were excluded from both the [CG18](#) catalog and the [K13](#) catalog.

### 4. Variable Catalog Census

#### 4.1. Ambiguous Blend Distribution

Of our 1143 catalog variables, 830 sources were identified as the primary variable source, while we were unable to identify an unambiguous primary for the remaining 313 variables within blended groups. In Figure 2, we illustrate the 2D projected spatial distribution of our primary variables (green circles) and our ambiguously blended variables (gray circles). A collection of ambiguously blended variables is observed near the core of NGC 2158. This is expected, given the low angular

### Variable Classification Distribution

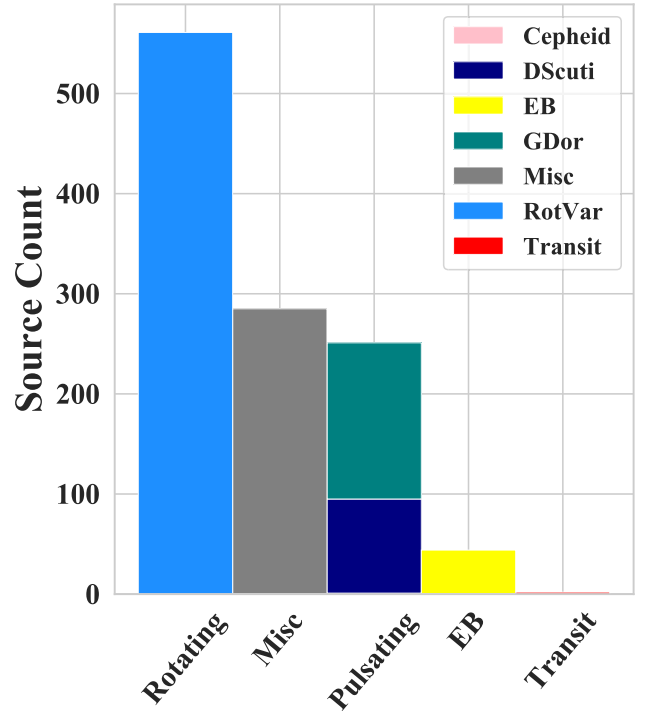


**Figure 3.** A stacked histogram illustrating the source count for our five variable classes: 561 rotational variables, 251 pulsating variables (primarily  $\gamma$  Doradus and  $\delta$  Scuti variables), 44 EBs, and 2 transiting exoplanet candidates.

separation of stars in this region, which results in enhanced blending.

#### 4.2. Classification Distribution

The variable classification distribution among our catalog variables is shown in Figure 3. Our identified variable classes are listed as follows: *Pulsating*, *Rotating*, *Misc*, *EB*, and *Transit*. Subclassification identifiers were used to more precisely distinguish variable type when such a distinction was possible. For example, an identified  $\gamma$  Doradus star is listed with the class identifier *Pulsating* and the subclassification identifier *GDor*. Rotating variables make up the most highly populated variable class group, containing 561 objects and comprising nearly half of all catalog variables. Pulsating variables make up the second most populated variable classification group, containing 251 sources. Nearly all our pulsating variables are  $\gamma$  Doradus and  $\delta$  Scuti pulsators. The 44 detected EBs make up 4% of our variable catalog, and our two exoplanet transit candidates make up 0.2%. We review the variable class distribution of cluster-affiliated sources in Section 4.3.

The 2D projected spatial distribution of our catalog variables is shown in Figure 4. Candidate transiting exoplanets are encircled in red, candidate EB sources are encircled in yellow, and rotating/pulsating variable sources (as well as indeterminate or *Misc.* sources) are encircled in blue.

#### 4.3. Cluster Membership Distribution

For the cluster membership distribution analysis, we consider “high-probability members” as sources with  $P_m > 0.9$  and “probable members” as sources with  $P_m > 0.5$ . A total of 740

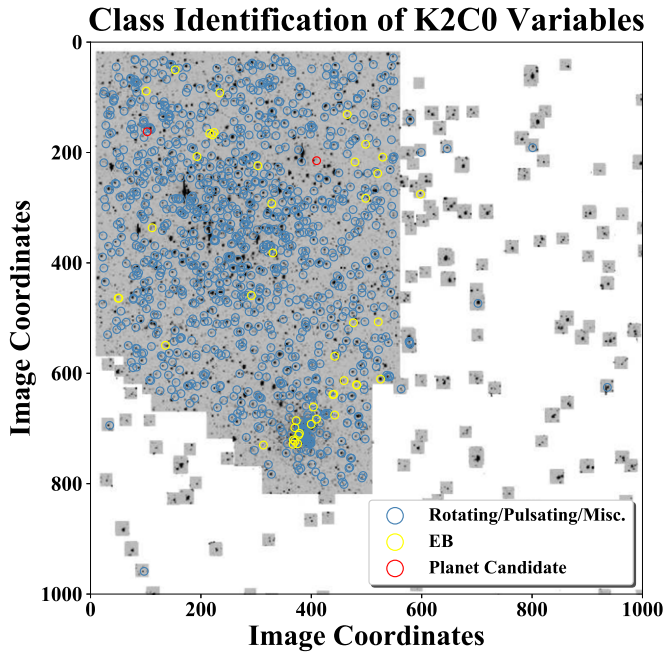


**Figure 4.** Two-dimensional projected spatial distribution of our catalog variables. Sources are color-coded to reflect variable classification.

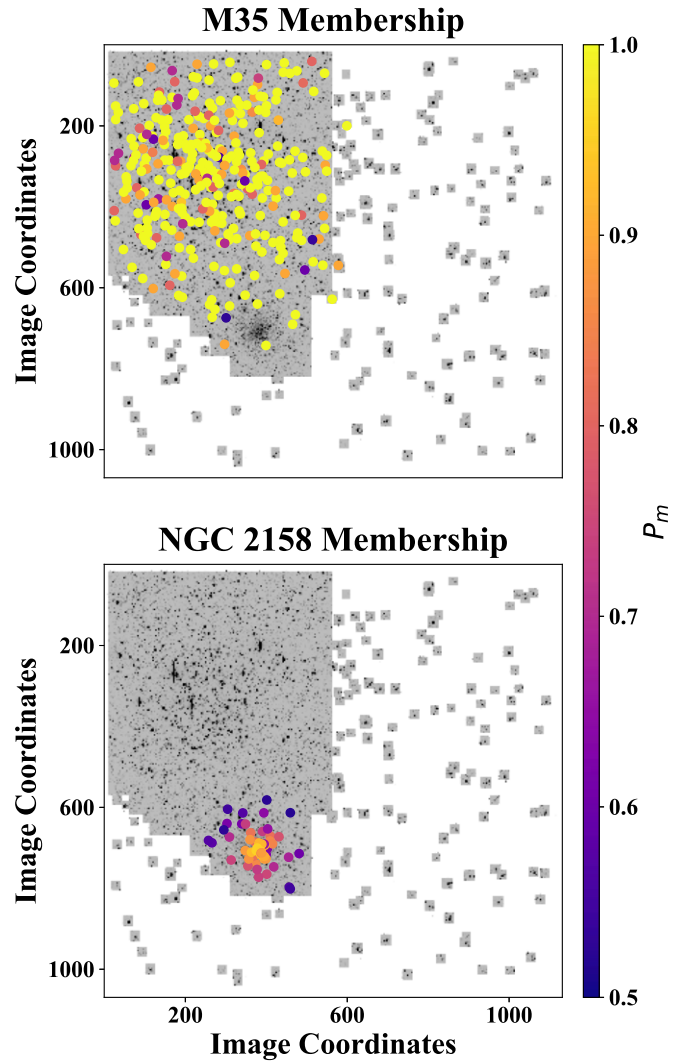
variables were designated as field sources ( $P_m < 0.5$  for both clusters). The 2D projected spatial distribution for probable cluster members is shown in Figure 5. The color corresponds to membership probability, ranging between 0.5 and 1. M35 members are well-dispersed across the super stamp, while the NGC 2158 variables are positioned close to the cluster core.

Table 2 summarizes the number of cluster members found among our 1143 catalog variables for both probable members and high-probability members. Within the catalog are 331 M35 cluster members (74% are high-probability members) and 56 NGC 2158 cluster members (21% are high-probability members). Of the M35 variables, 274 were designated as primary sources (not ambiguously blended). Of the NGC 2158 catalog variables, 34 were designated as primary sources.

In Figure 6, we illustrate the variable classification distribution for members of M35 (top) and members of NGC 2158 (bottom). The cluster variables consist of EBs, pulsating variables, rotating variables, and those of indeterminate type. No cluster-associated transiting exoplanet candidates were found. For the cluster M35, we found one EB candidate, 232 rotating variables, 51 pulsating variables (18  $\delta$  Scuti variables and 33  $\gamma$  Doradus variables), and 47 variables of indeterminate type. For the cluster NGC 2158, we found five EBs, 16 rotating variables, 13 pulsating variables (two  $\delta$  Scuti variables and 11  $\gamma$  Doradus variables), and 22 variables of indeterminate type. The proximity of M35 results in a greater sensitivity to low amplitude variations, which accounts for the larger number of total variables. NGC 2158 is richer in the total stellar count; this accounts for the greater number of EBs, which generally display large amplitude variations.

#### 4.4. Color–Magnitude Distribution

In Figure 7, we illustrate the color–magnitude distribution of our catalog variables in  $V-I$  versus  $V$  format. Our original 3960 K2C0 LCs are plotted as *gray* points in the background of each of the CMD panels. Our 331 probable M35 variables are shown



**Figure 5.** The spatial distribution of cluster members ( $P_m > 0.5$ ), color-coded to reflect membership probability. M35 members are shown in the *top panel* and NGC 2158 members are shown in the *bottom*. High-probability M35 members ( $P_m > 0.9$ ) are found across the K2C0 super stamp, while high-probability NGC 2158 members are positioned closer to the cluster core.

**Table 2**  
Census Data for Our Cluster Variables

	M35	NGC 2158
	$P_m > 0.5$	
$N_{m,var}$	331	56
$N_{m,prim}$	274	34
	$P_m > 0.9$	
$N_{m,var}$	245	12
$N_{m,prim}$	203	3

**Notes.** Results are listed for sources with  $P_m > 0.5$  (*top*) and for high-probability members with  $P_m > 0.9$  (*bottom*). The number of cluster members found in our K2C0 variable catalog is given in the column  $N_{m,var}$ . The number of primary members (not blends) in the variable catalog is given by  $N_{m,prim}$ .

in the first column, our 56 NGC 2158 probable variables are shown in the second column, and our 740 field sources are shown in the third column. Sources identified as primary variables are shown in the top row and ambiguous blends are

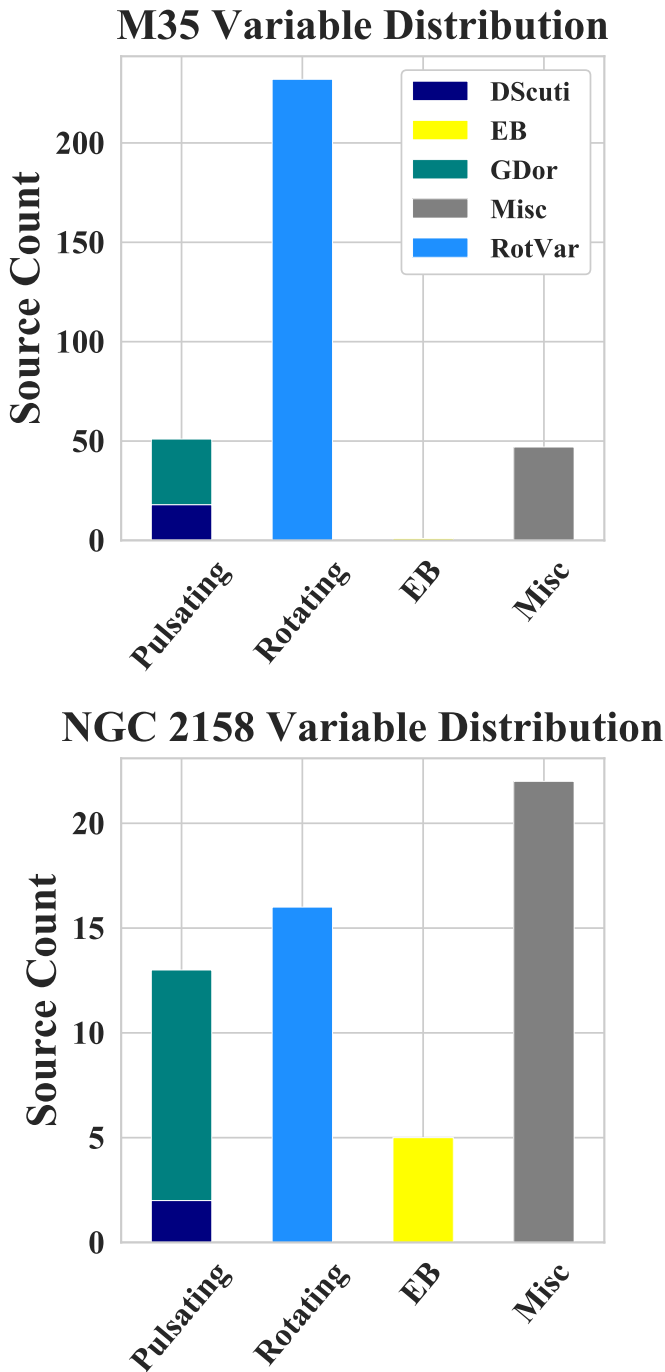


**Figure 6.** Variable classification distribution for probable M35 members (*top panel*) and probable NGC 2158 members (*bottom panel*). Note the differences in y-axis bounds to account for the fact that our catalog contains  $6\times$  more M35 members than NGC 2158 members. M35: one EB, 51 pulsating variables, and 232 rotating variables. NGC 2158: five EBs, 13 pulsating variables, and 16 rotating variables.

shown in the bottom row. We illustrate the class of rotating variables as *blue points*, pulsating variables as *green diamonds*, EB candidates as *yellow triangles*, and transiting exoplanet candidates as *red crosses*. Note that there is some overlap between the open clusters and the field sources. These data are in good agreement with the cluster CMD distributions produced using photometry data from Carraro et al. (2002; for M35) and Barrado y Navascués et al. (2001; for NGC 2158). We obtained

the comparison photometry data from the open cluster database, WEBDA.<sup>7</sup>

Our M35 member variables range in V-band magnitude from 10th mag to 18th mag. A total of 274 M35 variables are primary sources (top row), while the remaining 57 variables are ambiguous blends (bottom panel). The sole M35 EB is ambiguously blended with a field source (the field source has  $P_m = 0$ ). The vast majority of M35 cluster member variables are classified as rotating variables (232 sources) and pulsating variables (51 sources).

NGC 2158 variables range in V-band magnitude from 13th mag to 18th mag; a narrower magnitude range than M35, which is unsurprising given the difference in age, turn-off mass, and distance. This CMD is much broader than its M35 counterpart, likely caused by an overestimate of membership probability given the cluster’s low proper motion. A total of 34 NGC 2158 variable members in our variable catalog are identified primary sources (top row), while the remaining 22 variables are ambiguous blends (bottom panel). We observed five EBs with membership probabilities ranging between 52% and 85%; one is an ambiguous blend. Similar to our findings for M35, the vast majority of our probable NGC 2158 members are rotating variables (16) and pulsating variables (13).

#### 4.5. Period–Magnitude Distribution

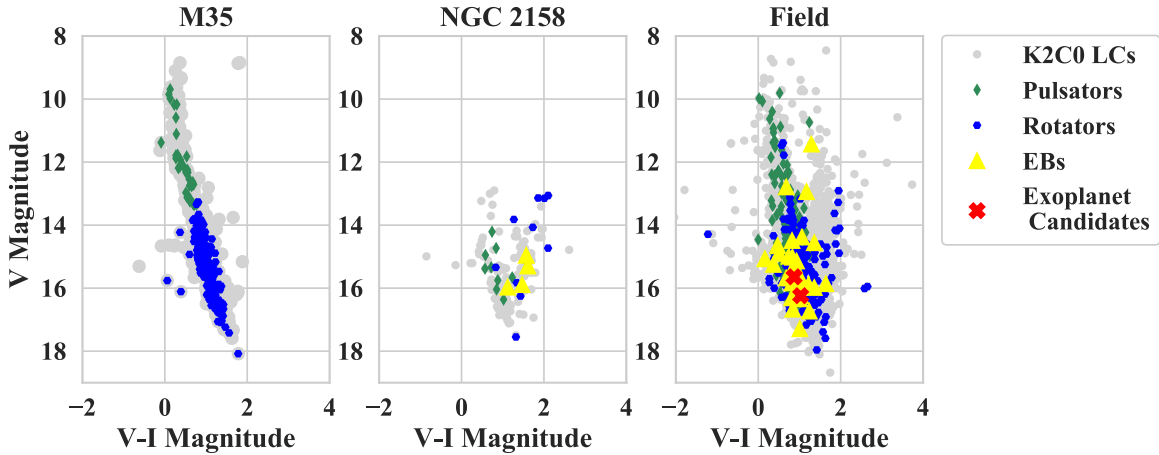
The period–magnitude distribution among our M35 primary variables is shown for members with  $P_m > 0.9$  in Figure 8 (ambiguous blends are excluded from the figure). Along the top x-axis, we list the corresponding estimated stellar masses. The stellar masses in this figure were calculated by fitting an isochrone to the stellar cluster parameters. These parameters included age, metallicity, and the absolute V source magnitude, which is dependent upon distance and reddening estimates. The cluster parameters used are listed in Section 2.1 (M35).

The source intensity is measured in the broad *Kepler* bandpass, known as the *Kepler magnitude* ( $K_p$ ). The M35 primary variables range in  $K_p$  from 9.7 to 17.2 mag. The sources are color-coded to indicate variable class as follows: rotating variables (*blue*), pulsating variables (*green*), and indeterminate variables (*gray*). The pulsating variables represent the brightest cluster class. All M35 pulsating variables have  $K_p \leq 14.8$  mag and  $P \leq 3.3$  days. The M35 rotating variables occupy nearly the full  $K_p$  magnitude range, with the majority of the faintest M35 catalog sources being of this class. The rotating variables are also spread across a wide range of source periods, ranging from 0.4 to 10.6 days. An obvious rotation period–magnitude relation is observed among our M35 variables, which is a chief rotation feature of intermediate-aged stars. While most of the rotating sources fall near the rotation period–magnitude relation, some are found far from this locus. Those falling below the sequence may be more rapidly rotating cluster members, which are commonly seen in young clusters like M35. Rapidly rotating cluster sources may be tidally spun up, or simply the rapidly rotating tail of a distribution that has yet to converge onto the sequence. Sources located above the rotation period–magnitude relation are likely explained by one of the following causes: (a) the target has an incorrect period estimate, (b) the target is blended with an unresolved source,

<sup>7</sup> The Open Cluster database WEBDA is available at <http://www.univie.ac.at/webda/webda.html>.



## Primary Sources



## Ambiguously Blended Sources

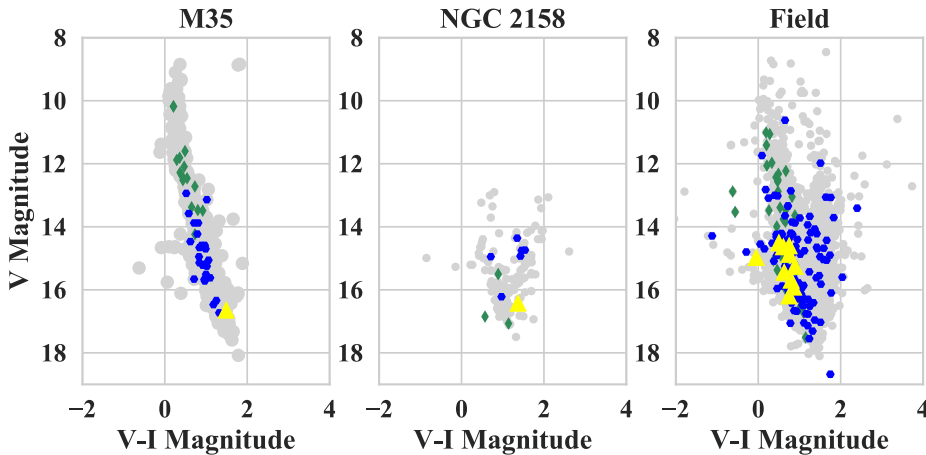


**Figure 7.**  $V-I$  vs.  $V$  CMDs for primary sources (top row) and blended sources (bottom row) in M35 (first column), NGC 2158 (second column), and the field (third column). The  $V$  and  $I$  measurements were obtained using UCAC4. The *gray points* in each panel depict sources from our full set of K2C0 LCs.

(c) the target is misclassified, or (d) the target is a field source with a proper motion very similar to that of M35.

Unfortunately, there are too few sources to make such a plot for NGC 2158 primary members, as many are blended or have lower membership probabilities. Using the membership threshold of  $P_m > 0.5$ , we found that a relationship between the rotation period and stellar mass is not evident for this system. This is expected, given that the detected NGC 2158 variables are brighter than the MSTO—and are therefore not representative of the cluster main sequence.<sup>8</sup>

### 5. Comparing Our Results to Other Surveys

We compared our variable catalog to the five catalogs that are described in Sections 5.1–5.5. To identify matches within each of the catalogs, we used *Astropy* to perform a search for the nearest neighbors, comparing the periods and associated harmonics for each of the potential matches. In the following sections, we describe the catalog contents and the number of comparable sources. Comparable sources are those that are not associated with one or more of the following conditions: (a) the

source is located within empty regions of the K2C0 super stamp (no match with a separation radius of  $r_s < 5''$ ), (b) the source did not have a counterpart in the UCAC4 catalog and was therefore not in our raw LC sample, (c) the source is outside our period bounds, and (d) the source was outside our  $V$  magnitude bounds.

#### 5.1. VSX Catalog Classification Comparison

We compared our catalog variables with the variables listed in VSX (Watson et al. 2006, 2017). The VSX catalog contains 528,037 variables spread throughout the northern and southern hemispheres. There was very little overlap between our catalog variables and the VSX catalog sources. Only 26 VSX variables were located within the  $1.5 \times 1.5$  degree field centered on M35. Of these 26 VSX variables, there were eight comparable sources. We identified three unique matches when compared with our catalog. All the matched sources were separated by less than a milliarcsecond. They also all possessed nearly identical periods when provided (less than 0.2% difference) and were classified as the same variable type. The VSX matches consisted of HN Gem, the hybrid source HD 252154 (which displays LC characteristics reminiscent of both  $\delta$  Scuti and

<sup>8</sup> The NGC 2158 MSTO mass is  $1.3 M_\odot$  (Carraro et al. 2002).

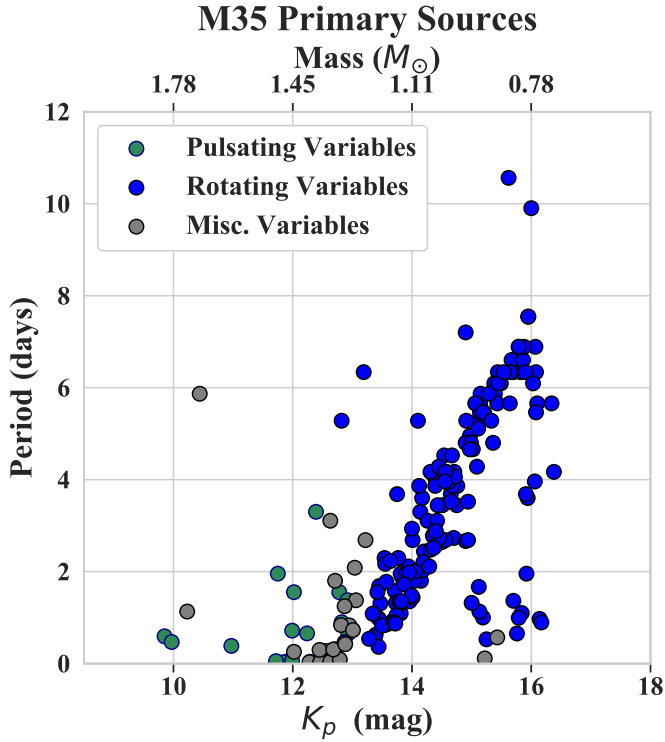


**Figure 8.** The well-correlated rotation period–magnitude relation among our M35 variables. We illustrate high-probability members with  $P_m > 0.9$ . This is a chief rotation feature of intermediate-aged stars. The upper x-axis displays the corresponding masses, produced using isochrone fits to the cluster parameters (age and metallicity) and the absolute  $V$  magnitude.

$\gamma$  Doradus variables), the  $\delta$  Cepheid variable V0371 Gem, and the  $\delta$  Scuti source V0392. The VSX identifiers for all the matched sources are provided in the *Column 70 (Match5)* of our variable catalog.

### 5.2. Meibom M35 Variability Comparison

Meibom et al. (2009, hereafter M09) performed a detailed analysis of the period–color relationship of rotating stars in M35 using data from the WIYN 0.9 m telescope. In addition to conducting a five-month photometric survey, the authors reviewed data from a decade-long radial-velocity survey, which resulted in the production of a variable catalog listing rotation periods, cluster membership, and binarity for 441 sources within a  $40' \times 40'$  field centered on M35. They concluded that 310 of these rotators were probable cluster members ( $P_m > 0.5$ ).

Of these 441 M09 variables, there were 255 comparable sources. We identified 189 unique matches when compared with our catalog. All the matched sources were separated by less than 10 mas. The unmatched M09 variables tended to have longer periods. The median period for unmatched sources was  $\bar{P} = 5.0$  days, while the median period for matched sources was  $\bar{P} = 3.3$  days. The M09 variable matches are displayed as *yellow circles* in the first panel of Figure 9. The *dotted lines* in the figure depict the relation  $P_{\text{other}} = \alpha \times P_{\text{MSF}}$ , where  $\alpha = [0.25, 0.5, 1, 1.5, 2]$ ,  $P_{\text{other}}$  is the rotation period listed in for the match in the M09 catalog. Some of the unmatched M09 sources were omitted from our catalog as duplicate secondary sources or due to a lack of compelling periodicity upon inspection. The M09 identifiers for

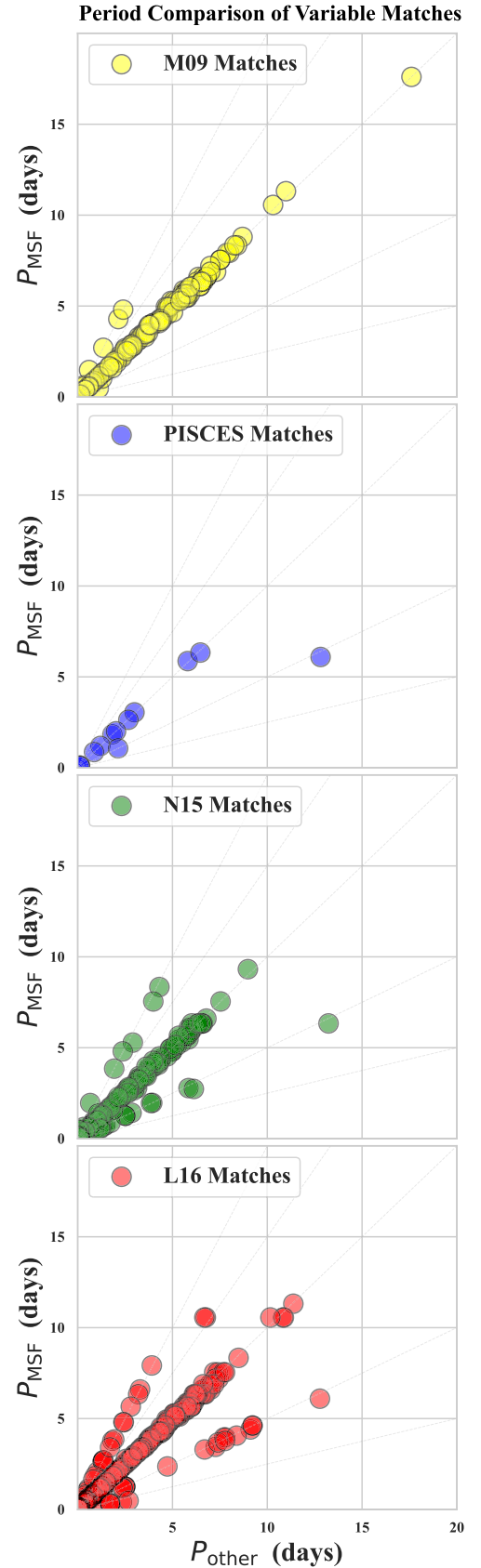


**Figure 9.** Comparison of reported periods for matches found in prior variable catalogs. The *dashed lines* denote the relation  $P_{\text{MSF}} = \alpha \times P_{\text{other}}$ , where  $\alpha = [0.25, 0.5, 1, 1.5, 2]$  and  $P_{\text{other}}$  is the period reported in the respective search catalog.

matches are provided in *Column 68 (Match3)* of our K2C0 variable catalog. Using our membership prescription, as outlined in Section 3.4, we found that 54% of uniquely matched sources have an M35 membership probability of  $P_m > 0.5$ .

### 5.3. PISCES NGC 2158 Variability Comparison

The first variability search conducted on NGC 2158 was led by Mochejska et al. (2004) as part of the Planets in Stellar Clusters Extensive Search (PISCES). This photometric survey spanned 20 nights (2003 January 3 to March 11) and observations were taken with the 1.2 m telescope at Fred Lawrence Whipple Observatory. This group employed an image subtraction technique, achieving  $\sim 5$  millimag precision. While the total time span of the observations is close to our observation window, the PISCES data set is discontinuous, with a daily  $\sim 16$  hr break in the data. A total of 57 variable stars were found, all exhibiting low-amplitude variability, including 34 EBs and five  $\delta$  Scuti variables. A second PISCES campaign was performed in 2006, consisting of 260 hr of photometry taken over the course of 59 nights (Mochejska et al. 2006). In this second analysis, 40 new variable stars were found, bringing the total number of detected variables to 97 (two sources have since been omitted from this catalog). The cumulative observation window for both campaigns spanned 13 months.

The second campaign resulted in the detection of TR1, a hot Jupiter candidate with an expected radius of  $1.66 R_J$  and a period of 2.3629 days. Higher-accuracy LCs were required to better constrain the radius and period. Using a high-resolution catalog and a neighbor subtraction technique, Libralato et al. (2016) was able to make improved measurements of the depth of the eclipses for this source. At the 2018 January Dwarf Stars and Clusters with K2 conference, Nardiello (co-author of Libralato et al. 2016) presented results indicating that TR1 is likely an EB. TR1 is below our magnitude threshold ( $K_p \simeq 18.35$  mag), so it is not present in our catalog.

Of these 95 PISCES variables, there were 22 comparable sources. We identified 13 unique matches when compared with our catalog. All the matched sources were separated by less than a milliarcsecond. The variable matches are shown as *blue points* in the second panel of Figure 9. Not all matched variables were classified in the same manner. This classification discrepancy is unsurprising, as the PISCES team noted that more than half of the designated EBs may be ellipsoidal variables. The PISCES identifiers for matches are provided in the *Column 69 (Match4)* of the K2C0 variable catalog. We found that eight matches are probable cluster members (one of which is associated with M35).

### 5.4. Nardiello M35 and NGC 2158 Comparison

Nardiello et al. (2015, hereafter N15) surveyed open clusters M35 and NGC 2158 as part of the The Asiago Pathfinder for HARPS-N program. They employed ground-based, high-precision ( $\sim 5$  millimag), fast-cadence ( $\sim 3$  min), multiband photometric data. To mitigate blending, the group implemented a point-spread function (PSF) neighbor subtraction technique. They found a total of 519 variables; 273 of these variables were new discoveries. No candidate exoplanetary transiting sources were found in this study.

Of the 519 N15 catalog variables, there were 283 comparable sources. We identified 215 unique matches when compared with our catalog. All the matched sources were separated by less than a milliarcsecond. As in the case of the M09 catalog, the unmatched sources tended to have longer periods. The median period for

unmatched N15 sources was  $\bar{P} = 8.5$  days, while for matched sources it was  $\bar{P} = 2.3$  days. The matches are shown in the third panel of Figure 9 (*green points*). The N15 identifiers for matches are provided in the *Column 67 (Match2)* of the K2C0 variable catalog. We did not always designate the same variable class for our matches. We omitted a detailed comparison of our catalog with the K2C0 variable search conducted by LaCourse et al. (2015), which did not implement image subtraction or PSF neighbor subtraction methods. These results did not offer any information relevant to our catalog that had been omitted by N15.

### 5.5. K2-specific M35 and NGC 2158 Comparison

The most direct comparison of our results can be made with the variable catalog generated by Libralato et al. (2016, hereafter L16). This group conducted a deep search on the K2C0 super stamp using a PSF neighbor subtraction technique, as described in Nardiello et al. (2015). They employed the high angular resolution Asiago Input Catalog (AIC), compiled from observations made by the Asiago Schmidt Telescope. They generated a catalog of 2848 variable stars. Nearly 2000 sources are listed as *candidate variables*; 978 are flagged as “highly probable blends” and/or variables that were difficult to classify. Variability periods were not provided for 380 catalog sources, which also prevented us from making a direct comparison.

Of the 2133 L16 catalog variables, there were 730 comparable sources. This small subset of comparable sources was largely due to their ability to probe to fainter magnitudes. The AIC reaches magnitudes of  $K_p \sim 24$  mag, while our minimum brightness was  $K_p \sim 17$  mag. Another cause was the lack of published periodicity estimates within the L16 catalog. Moreover, although we employed the same data set, we only use data obtained when the instrument was in fine-pointing mode, which comprised roughly half of the campaign window. Therefore, our period bounds are narrower.

Of the 730 comparable sources, we identified 545 unique matches when compared with our catalog. All the matched sources were separated by less than a milliarcsecond. Most of the unmatched sources were omitted from our catalog as duplicate secondaries. In fact, 33% of the unmatched L16 variables were listed as being either probable blends or difficult to classify. The matches are shown in the bottom panel of Figure 9 (*red points*). The matched sources tended to be slightly brighter. For the unmatched L16 sources, the median was  $V = 15.6$  mag, while this value was  $V = 15.1$  mag for matched sources. Unmatched sources tended to display longer periods of variability. The median period for unmatched L16 variables was  $\bar{P} = 4.6$  days, while the median period of matched variables was  $\bar{P} = 1.5$  day. We illustrate the period and magnitude distributions for matched versus unmatched sources in Figure 10.

## 6. New Variables

We revealed 523 new variables. These sources were not identified in any of the variable searches described in Section 5. Our new variables include two field candidate transiting exoplanets, ten EBs, 55 variables of indeterminate type, 88  $\delta$  Scuti variables, 137  $\gamma$  Doradus variables, and 141 rotational variables. The exoplanet candidates and EBs are described in further detail in Sections 7 and 8, respectively. The fourteen new rotational variables identified as probable NGC 2158 members are particularly valuable, given that rotation period measurements are scarce among older stars.



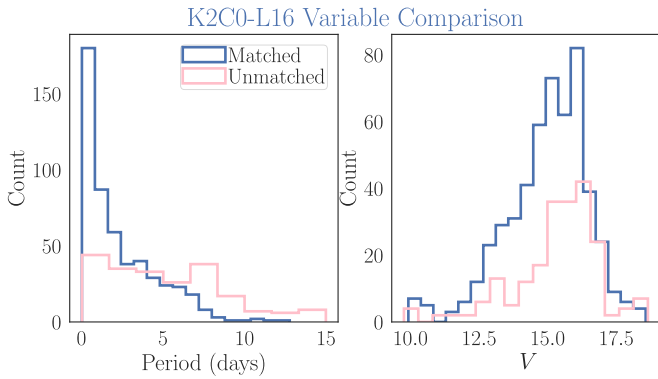


**Figure 10.** Distributions of the period variability and  $V$  magnitude for matched (blue) and unmatched L16 variables (pink). Unmatched sources tended to possess longer variability periods, with  $\bar{P} = 4.6$  days for unmatched variables and  $\bar{P} = 1.5$  days for matched variables. Matched sources tended to be slightly brighter ( $\bar{V} = 15.1$  mag) than unmatched variables ( $\bar{V} = 15.6$  mag). This same tendency was seen when comparing our variables to the M09 and N15 catalogs.

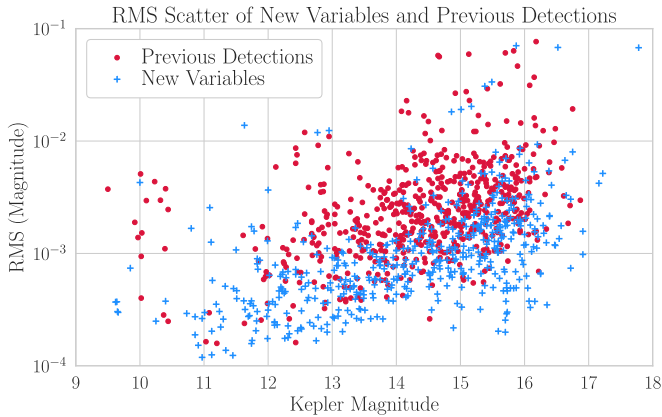


**Figure 11.** The TFA-corrected rms LC scatter for previously detected variables (red points) and newly detected variables (blue crosses). We define the rms scatter as the  $3.5\sigma$  clipped 68.27th percentile of the distribution about the median value of the LC magnitude. Using bin sizes of one mag, the median rms for previous detections is a factor of 1.8–2.5 larger than that of the new detections. This factor is least for stars of 14–15 mag and greatest for stars of 10–11 mag ( $K_p$ ).

The newly identified variables tended to have smaller amplitude variations than the variables found in prior searches. Previously identified variables had a mean oscillation amplitude of  $\sim 13$  millimag, while newly identified variables displayed a mean oscillation amplitude of  $\sim 4$  millimag. Figure 11 depicts the TFA-corrected LC rms scatter for previously detected sources (red points) to that of the newly detected variables (blue crosses). The rms scatter is defined here as the  $3.5\sigma$  clipped 68.27th percentile of the distribution about the median value of the LC magnitude. Comparing the TFA-corrected rms in bin sizes of one mag, we observed that the median rms of previous detections is a factor of 1.8–2.5 larger than that of our new detections. This factor is smallest for stars with  $K_p$  magnitude of 14–15 mag and greatest for stars with  $K_p$  of 10–11 mag. The period and  $K_p$  magnitude distributions of our new variables were similar to that of the unmatched variables. The mean values of both distributions display  $<3\%$  difference.

Our new variables are generally lower in S/N. We found a median LS S/N ratio of 118 for new variables, as compared to

**Table 3**  
UCAC4-573-025379

HATID	HAT-264-0137730
R.A. (degrees)	92.428917
Decl. (degrees)	24.528807
$K_p$ (mag)	15.4
<i>Gaia</i> Source ID	3426297073623137024
$T_{\text{eff}}$ (K)	$4896 \pm 216$
$L_*$ ( $L_\odot$ )	$0.257 \pm 0.019$
$R_*$ ( $R_\odot$ )	$0.70 \pm 0.07$
$A_G$	$0.68 \pm 0.14$
$E(\text{BP-RP})$	$0.34 \pm 0.08$
$\varpi$ (mas)	$1.401 \pm 0.047$
Distance (pc)	$714 \pm 25$
pmra (mas/r)	$-5.608 \pm 0.084$
pmdec (mas/r)	$-6.437 \pm 0.073$
Period (days)	1.256774
Epoch (BJD)	2456775.234
$t_{\text{depth}}$ (millimag)	2.9
$t_{\text{dur}}$ (hr)	1.12
$R_p$ ( $R_J$ )	$1.1 \pm 0.1$
$R_p/R_*$	$0.055 \pm 0.05$
$a/R_*$	$8_{-1}^{+4}$
Inclination	$87^\circ \pm 3^\circ$

552 for previously identified variables. S/N was computed using Astrobase and is described in Section 3.1.2. About 40% of the newly detected variables are ambiguous blends for which we cannot distinguish a primary source. In contrast, ambiguous blends represented 27% of the previously identified variable population. Using information from *Gaia* DR2, we find that our new variables tend to be almost twice as distant and  $2.5\times$  more luminous.

## 7. Exoplanet Candidates

Our two transiting exoplanet candidates are new variables. They are both probable field sources. Both have been identified as primary sources (not blended). Information is provided for each of them in Tables 3 and 4, respectively. Their phase-folded LCs are shown in Figures 12 and 13. In addition to the *Gaia*-derived parameters, which are listed in the central panel of the table, we list system parameters obtained from our BLS analysis using VARTOOLS and Astrobase. We also list parameters obtained from transit modeling with BATMAN (Bad-Ass Transit Model cAlculationN; Kreidberg 2015), a Python package that analytically calculates the LC using the methods described in Mandel & Agol (2002).

### 7.1. UCAC4-573-025379

Our BLS periodogram search revealed a transiting exoplanet candidate with a period of 1.256774 days for the variable UCAC4-573-025379. The phase-folded LC for this source is composed of 1390 cadences and is shown in the top panel of Figure 12. The residuals after subtracting the best-fit model from the data are shown in the bottom panel. The red line denotes the zero point for residuals. The measured transit depth was 2.9 millimag, and the transit duration was measured as 0.05 days (1.12 hr). The associated star–planet parameters are listed in Table 3. The host star has a median brightness of  $K_p = 15.4$  mag. *Gaia* DR2 measurements suggest that the star

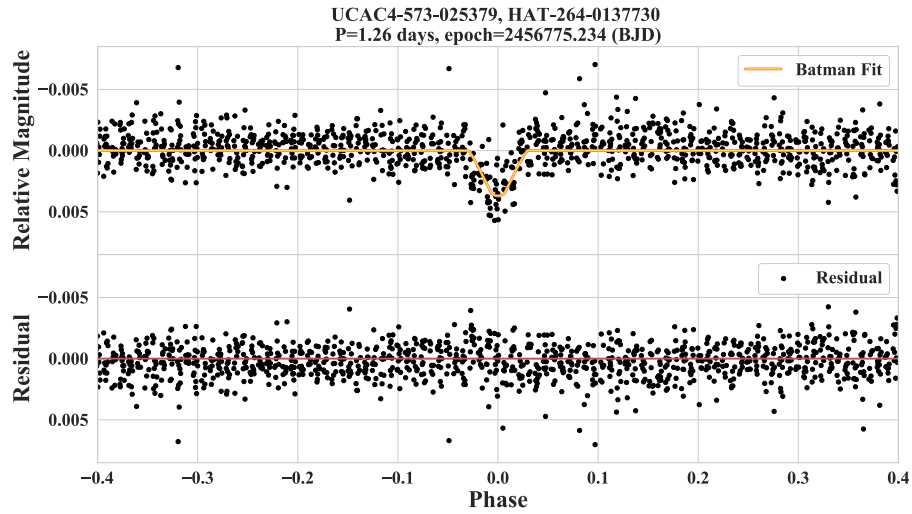


**Figure 12.** *Top:* phase-folded light curve for UCAC4-573-025379. This is a K-type field dwarf exhibiting a 2.9 millimag transit indicating a planet of  $R_p = 0.35 \pm 0.04 R_J$  with a period of 1.3 days. The system parameters are listed in Table 3. The BATMAN fit is shown in orange. *Bottom:* the residuals after subtracting the best-fit model from the data. This source is a new detection.

**Table 4**  
UCAC4-571-025423

HATID	HAT-264-0191717
R.A. (degrees)	92.448914
Decl. (degrees)	24.185612
$K_p$ (mag)	15.7
Gaia Source ID	3425513568507306112
$T_{\text{eff}}$ (K)	$3856 \pm 82$
$L_*$ ( $L_\odot$ )	$1.4 \pm 0.4$
$R_*$ ( $R_\odot$ )	$1.65 \pm 0.04$
$A_G$	$1.7 \pm 0.3$
$E(\text{BP-RP})$	$0.79 \pm 0.15$
$\varpi$ (mas)	$0.46 \pm 0.06$
Distance (kpc)	$2.2 \pm 0.3$
pmra (mas/r)	$1.2 \pm 0.1$
pmdec (mas/r)	$-2.5 \pm 0.1$
Period (days)	15.253697
Epoch (BJD)	2456791.47789
$t_{\text{depth}}$ (millimag)	2.2
$t_{\text{dur}}$ (hr)	0.77
$R_p$ ( $R_J$ )	$0.72 \pm 0.02$
$R_p / R_*$	$0.05 \pm 0.01$
$a/R_*$	$10 \pm 2$
Inclination	$87^\circ \pm 3^\circ$

is a foreground K dwarf with a radius of  $0.70 \pm 0.07 R_\odot$ . Our transit modeling suggests an orbiting planet of  $0.35 \pm 0.04 R_J$  at an inclination of  $87^\circ \pm 3^\circ$ . The star-planet parameters for this system are listed in Table 3.

UCAC4-573-025379 was matched with the *Gaia* source 3426297073623137024. The median *G* magnitude listed for this source match is 15.56 mag, which is in agreement with our *G* magnitude calculated using *B-V* Johnson-Cousins algorithm. *Gaia* provides an effective temperature measurement of  $T_{\text{eff}} = 4896 \pm 216$  K and a parallax measurement of  $\varpi = 1.401 \pm 0.047$  mas, indicating a distance of  $714 \pm 25$  pc. The source's parallax and proper motion measurements indicate that is not likely to be a cluster member. This source was excluded from the membership catalog generated by Cantat-Gaudin et al. (2018).

## 7.2. UCAC4-571-025423

Our BLS periodogram search revealed a transiting exoplanet candidate with a period of 15.253697 days for the variable UCAC4-571-025423. The phase-folded LC for this source is composed of 1388 cadences and is shown in Figure 13. Also shown in this figure are the residuals for our fit. The measured transit depth was 2.2 millimag and transit duration was 0.032 days (0.77 hr). Only two transits were used in the generation of this fit. Therefore, while this transiting exoplanet candidate cannot be ruled out, it is not extremely compelling and may turn out to be an unresolved binary or a false alarm. The host star has a brightness of  $K_p = 15.7$  mag. *Gaia* DR2 measurements suggest that the star is of the type G9IV with a radius of  $1.65 \pm 0.04 R_\odot$ . Our transit modeling indicates a planet of radius  $0.72 \pm 0.02 R_J$  at an inclination of  $87^\circ \pm 3^\circ$ . The position of this star on an HR diagram of stellar radius versus  $T_{\text{eff}}$  indicates that some of the stellar properties are probably in error, as this position is not covered by a stellar isochrone younger than the age of the universe. The star-planet parameters for this system are listed in Table 4.

We found a *Gaia* match for UCAC4-571-025351 (source ID 3425513568507306112). The mean *G* magnitude listed for the *Gaia* match is 16.12 mag, which is in agreement with our calculated *G* magnitude. The *Gaia* parallax measurement contained large error bounds, measuring as  $\varpi = 0.46 \pm 0.06$  mas, indicating a distance of  $2.2 \pm 0.3$  kpc. The *Gaia* parallax and proper motion measurements support the notion that this is likely a field star. The King model fit indicates that the source is unlikely to be an NGC 2158 cluster member ( $P_m < 1\%$ ). *Gaia* provides a wealth of stellar parameters, including the effective temperature, measured as  $T_{\text{eff}} = 3856 \pm 82$  K, stellar luminosity ( $L_* = 1.4 \pm 0.4 L_\odot$ ), the line-of-sight extinction in the *G* band ( $A_G = 1.67 \pm 0.3$ ), and a line-of-sight reddening of  $E(\text{BP-RP}) = 0.82 \pm 0.15$ .

## 8. Eclipsing Binaries

Of our 44 catalog EBs, ten are new detections and five are probable cluster members. The sole M35 cluster member EB is a new detection with a cluster membership probability of  $P_m = 0.8$ . Of the five NGC 2158 member EBs, one was a new detection and

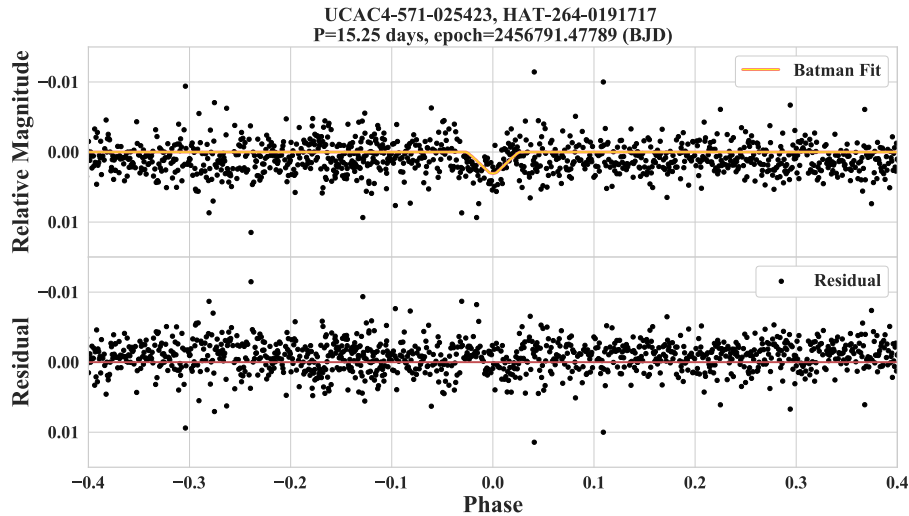


**Figure 13.** *Top:* phase-folded light curve for UCAC4-571-025423. This is a G9IV-type field star exhibiting a 2.2 millimag transit, suggesting a planet of  $R_p = 0.72 \pm 0.02 R_J$  with a period of 15.3 days. The system parameters are listed in Table 4. Only two transits were used in the creation of this light curve. This source may be an unresolved binary or a false alarm. The BATMAN fit is shown in orange. *Bottom:* the residuals after subtracting the best-fit model from the data. This source is a new detection.

three had been previously identified. Spectroscopic follow-up has not been conducted on any of the EBs in our variable catalog. We found four likely contact binaries; none of them are new detections and all are likely field members. Our catalog contact binaries include: UCAC4-571-025495, UCAC4-571-024709, UCAC4-573-025524, and UCAC4-571-025426. We found one semidetached EB, UCAC4-573-025574, which is a likely field source. One of the field EBs is highly eccentric. Five EB variables show signs of out-of-transit variation (OOTV), including UCAC4-571-024971, UCAC4-572-024695, UCAC4-573-025041, UCAC4-571-024688, UCAC4-572-024929. UCAC4-571-024971 also shows the characteristics of a reflection variable. Eight of our EB variables are eccentric (they display a secondary eclipse with a phase offset from 0.5). The eccentric EBs include the newly detected field source UCAC4-573-025427, as well as the previously observed sources UCAC4-571-025474, UCAC4-571-025548, UCAC4-572-025126, UCAC4-571-024775, UCAC4-571-024823, UCAC4-571-024819, and UCAC4-571-024606. UCAC4-571-024606 is a probable member of NGC 2158.

UCAC4-572-025138, the sole M35 EB source with  $P = 4.9$  days, is shown in Figure 14. This was a new detection with  $K_p = 15.7$  mag. This source displays an eccentric binary orbit. Unfortunately, the source is ambiguously blended with two field EBs. Cluster membership is supported by a proper motion analysis and the recent parallax provided by *Gaia* DR2 ( $\varpi = 1.241 \pm 0.090$  mas).

Our probable NGC 2158 member EBs are shown in Figure 15. They are illustrated in order of ascending period. These sources range in  $K_p$  from 14 to 15.7 mag. All the NGC 2158 EBs but UCAC4-571-024279 were previously observed by L16. The *Gaia* DR2 measured parallax for UCAC4-571-024645 suggests that this source may be more distant than the cluster. The distance estimate has large error bounds, however, ranging between 6 and 10 kpc. Stellar density estimates indicate that this source is an early K dwarf or late G dwarf. UCAC4-571-024279 is a new detection and the parallax for this source supports NGC 2158 cluster membership. UCAC4-571-024365 has a parallax measurement that supports cluster membership. This EB is ambiguously blended. A subtle OOTV can be seen in the phase-folded LC. UCAC4-571-024606 displays an eccentric binary orbit. The

### M35 Eclipsing Binary

HAT-264-0184370, UCAC4-572-025138  
RA=92.45984, DEC=24.39788,  $P_m=80\%$

period: 4.918830 d - epoch: 1942.345539

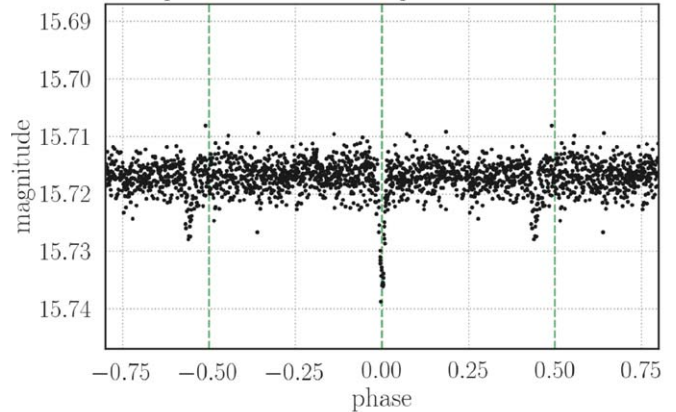


**Figure 14.** Phase-folded LC of our sole M35 EB source (UCAC4-572-025138) with  $P = 4.9$  days. Epoch is provided in BJD-2454833. Plotted along the y-axis is the  $K_p$  magnitude. This source is an ambiguous blend with two field EBs. This source displays an eccentric binary orbit. This M35 variable was not reported in prior analyses. Cluster membership is supported by *Gaia* DR2 proper motion and parallax measurements.

parallax of this source supports cluster membership. UCAC4-571-024827 has a low membership probability of  $P_m = 0.52$ , and may be a field source.

The phase-folded LCs for our population of field EBs are illustrated throughout Figures 16–20. We show only the brightest member of an ambiguously blended pair/group. Our field EBs are predominantly F- and G-type variables. The brightest field EB is UCAC4-571-025426, a subgiant of class G3, with  $L_* = 10 \pm 2 L_\odot$  and  $T_{\text{eff}} = 5200 \pm 200$  K. This is a semidetached EB that was observed in prior analyses. The second brightest EB, UCAC4-572-025069, is a G-class subgiant that shows some ellipsoidal variation. This source has  $L_* = 6.5 \pm 0.5 L_\odot$  and  $T_{\text{eff}} = 4950 \pm 50$  K. UCAC4-571-024330 is another EB with



## NGC 2158 Eclipsing Binaries

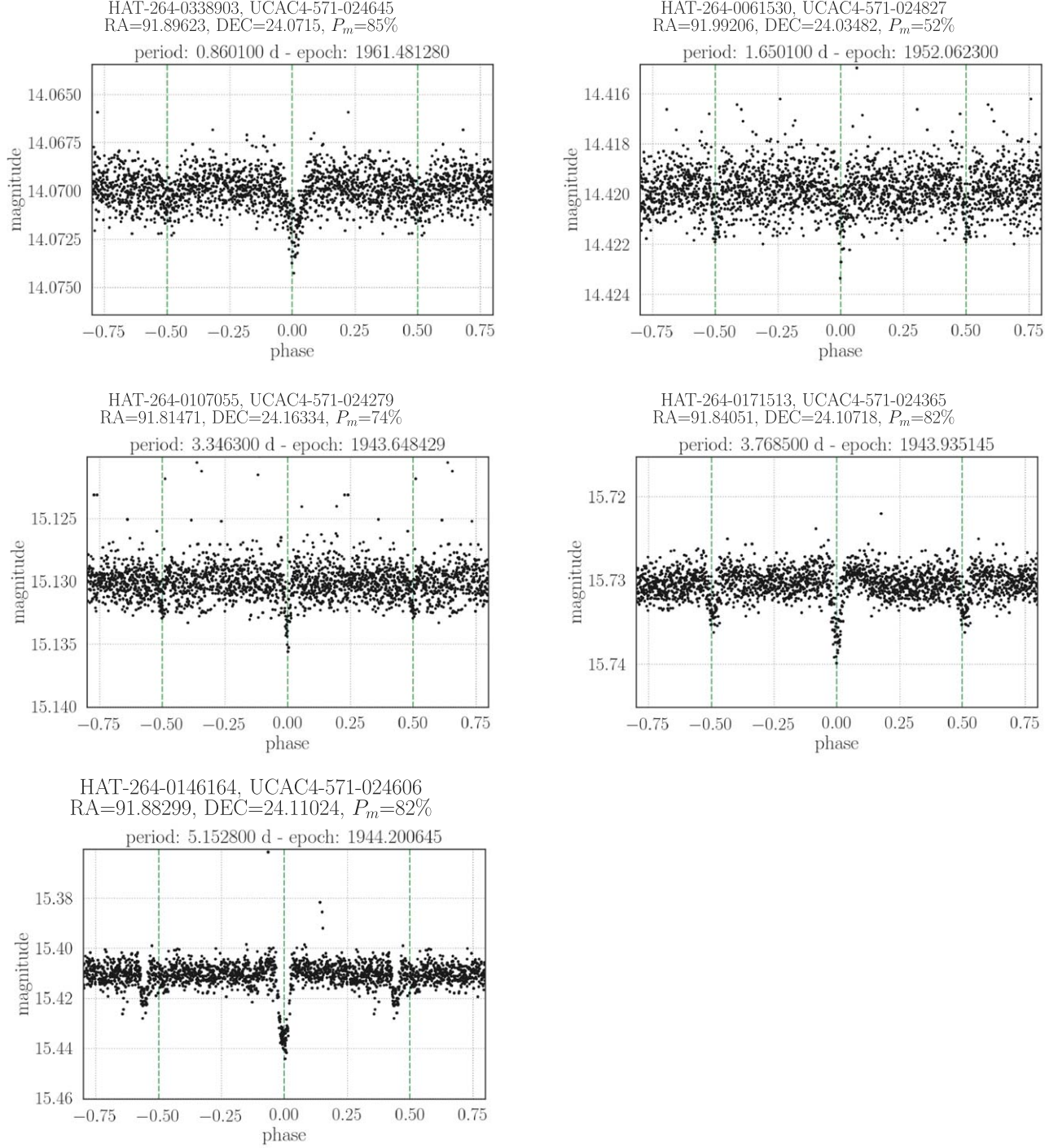


**Figure 15.** Phase-folded LCs for NGC 2158 associated EBs. Epochs are provided in BJD-2454833. The y-axis displays the  $K_p$  magnitude. The EB UCAC4-571-024279 (central left panel) is a new detection.

OOT ellipsoidal variation. The wiggles in this phase-folded LC imply spot modulation.

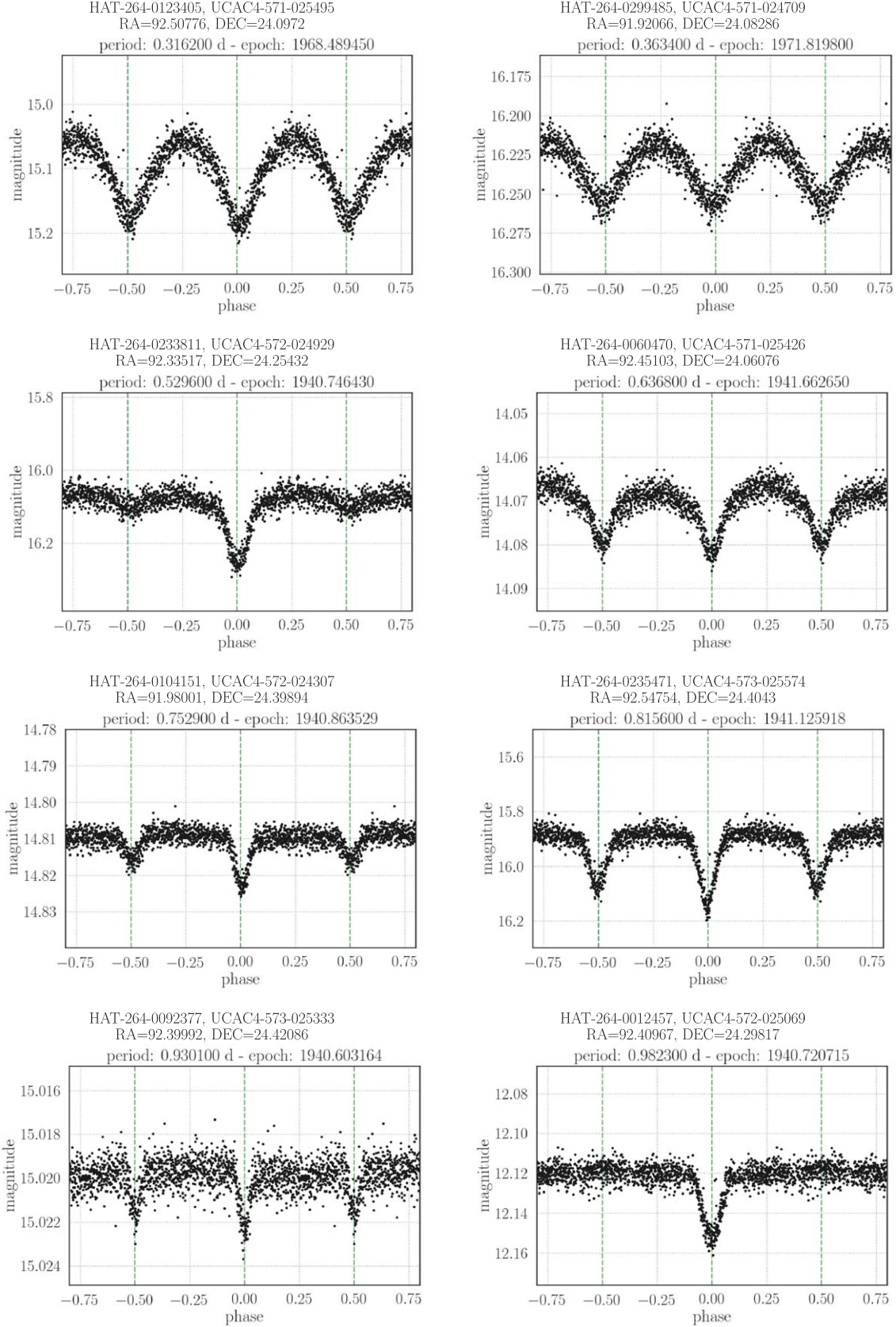
### 9. K2C0 $\delta$ Cepheid Variable

Throughout the *Kepler* mission, hundreds of Cepheid variables were observed (Molnár et al. 2018). Shown in Figure 21 is the phase-folded LC of the previously discovered

$\delta$  Cepheid variable, V0371 Gem, which is listed in the VSX catalog. This bright source ( $K_p = 9.906$  mag) is classified as K0 in spectral type. V0371 Gem is a probable field star. The source was also observed by L16 and N15. Our periodogram search reveals a period of 2.141186 days for this object. The VSX catalog lists a very similar value of  $P = 2.1371$  days.

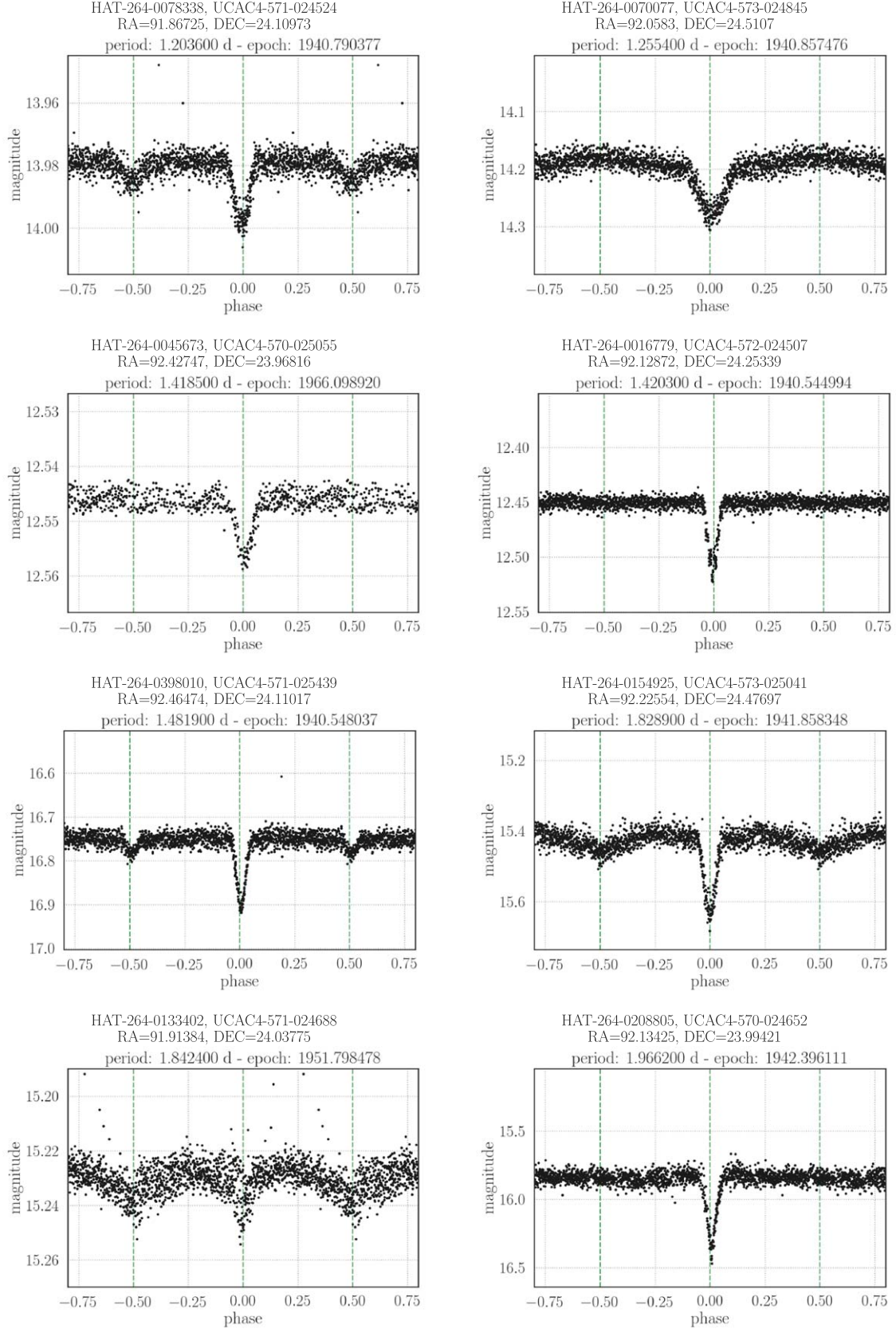
Filtering out the period and associated harmonics for  $P = 2.141186$  days, we also observed an overtone of  $P = 1.288193$

## Field Eclipsing Binaries



**Figure 16.** Phase-folded LCs for the EB variables associated with the field, displayed in ascending order of period. Epochs are provided in BJD-2454833. Plotted along the y-axis is the  $K_p$  magnitude of the source.

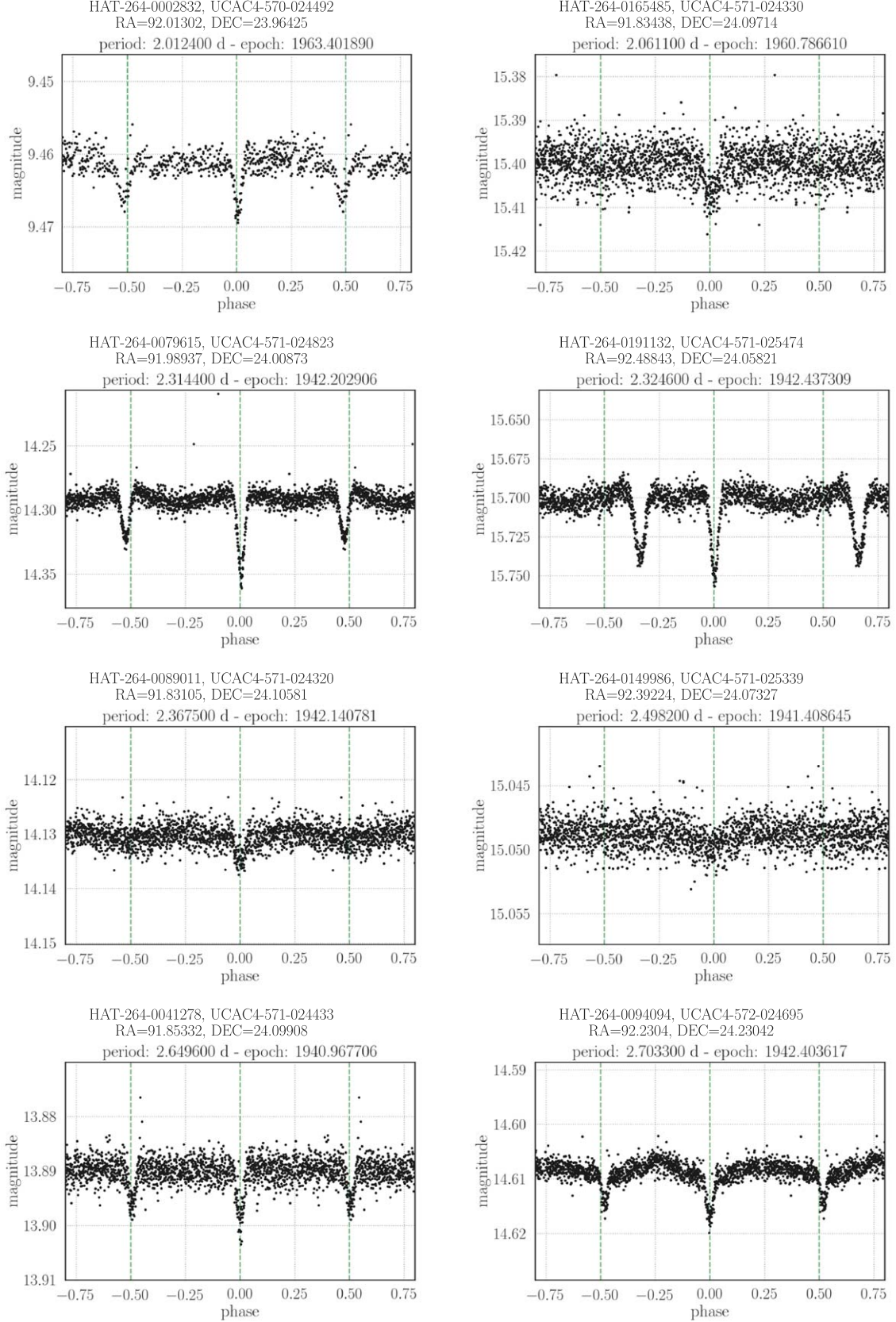
## Field Eclipsing Binaries



**Figure 17.** Phase-folded LCs for the EB catalog variables associated with the field, displayed in ascending order of period. Epochs are provided in BJD-2454833. Plotted along the y-axis is the  $K_p$  magnitude of the source.

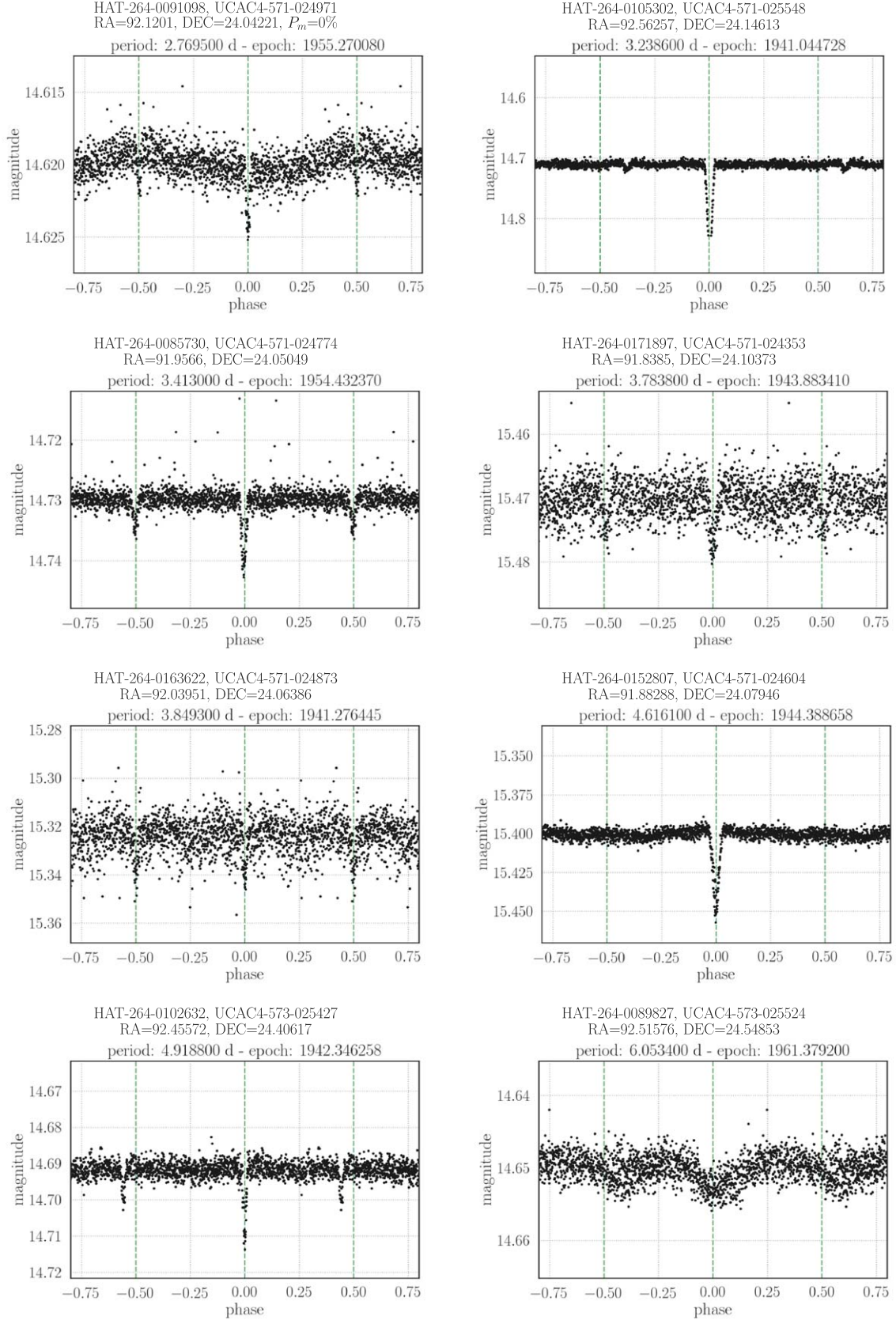


## Field Eclipsing Binaries



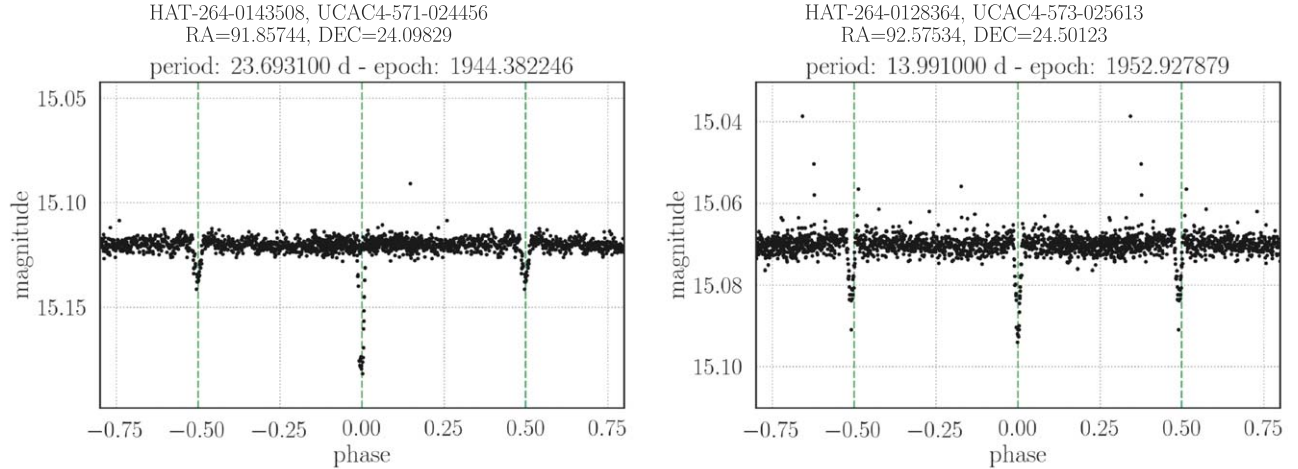
**Figure 18.** Phase-folded LCs for the EB catalog variables associated with the field, displayed in ascending order of period. Epochs are provided in BJD-2454833. Plotted along the y-axis is the  $K_p$  magnitude of the source.

## Field Eclipsing Binaries

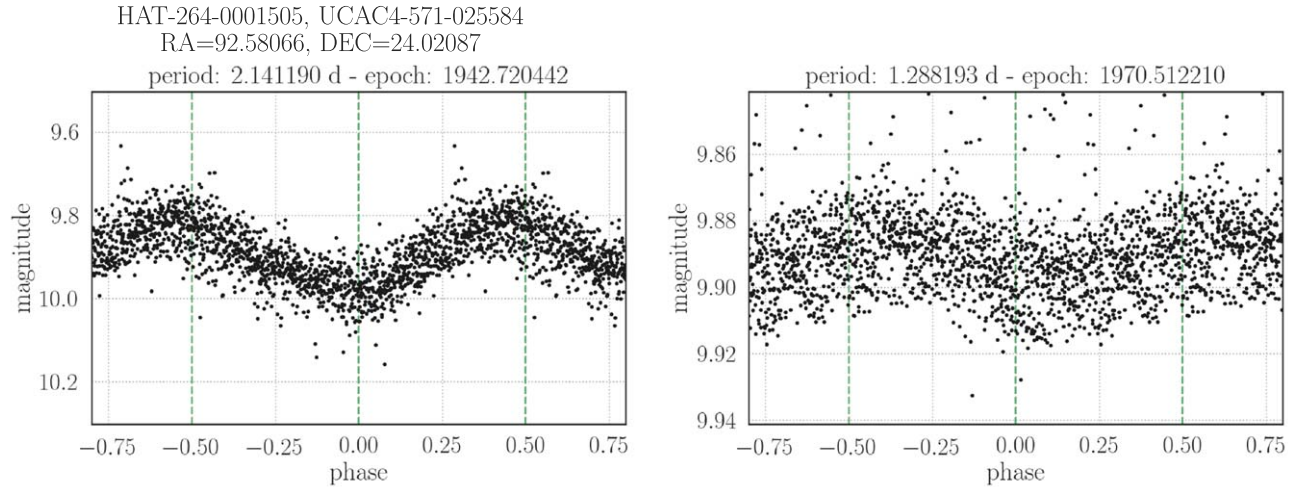


**Figure 19.** Phase-folded LCs for the EB catalog variables associated with the field, displayed in ascending order of period. Epochs are provided in BJD-2454833. Plotted along the y-axis is the  $K_p$  magnitude of the source.

## Field Eclipsing Binaries



**Figure 20.** Phase-folded LCs for the EB catalog variables associated with the field, displayed in ascending order of period. Epochs are provided in BJD-2454833. Plotted along the y-axis is the  $K_p$  magnitude of the source.

 $\delta$  Cepheid Variables

**Figure 21.** Phase-folded LC for V0371 Gem (UCAC4-571-025584), our catalog  $\delta$  Cepheid. The  $K_p$  magnitude is shown along the y-axis. *Left panel:* the strongest variability period at 2.141186 days. *Right panel:* the  $P = 1.288193$  day signal detected after filtering out the dominant period and associated harmonics. This source is not associated with either open cluster; this is confirmed by *Gaia* DR2 proper motion and parallax measurements. The period noted in the VSX catalog is 2.1371 days. The epoch is provided in BJD-2454833.

days, which has not been previously reported. The overtone is shown in the lower panel of Figure 21. Overtones have been noted in  $\delta$  Cepheid variables in the past. Double-mode Cepheids are a useful resource for testing stellar evolutionary and pulsation models (e.g., Buchler & Szabó 2007; Buchler 2008; Smolec & Moskalik 2010). V0371 Gem was matched in the *Gaia* DR2 data set with the source 3425495186047291136. The *Gaia* measured parallax indicates a distance of  $4 \pm 0.5$  kpc, similar to NGC 2158; however, both the 2D projected distance of the source from the cluster core and the proper motion measurements rule out cluster membership. For reference, the source's proper motion is calculated to be  $(\mu_\alpha \cos \delta, \mu_\delta) = (-0.54, -1.40)$  mas yr $^{-1}$ . *Gaia* analysis estimates a surface temperature of  $T_{\text{eff}} \sim 5000$  K, a radius of  $R_* \sim 40 R_\odot$ , and a luminosity of  $L_* = 818 \pm 166 L_\odot$ . No new Cepheids were found in our variable search, which is unsurprising given that the high luminosity of these sources often permits detection even when blending concerns are not mitigated.

## 10. K2C0 Rotational and Pulsational Variables

We illustrate the phase-folded LCs for three representative  $\delta$  Scuti variables, three representative  $\gamma$  Doradus variables, and three representative rotational variables from our K2C0 variable catalog. These represent highlighted examples, as many more are present in our catalog. The first two columns illustrate candidates observed in prior detections, while the final column illustrates a newly detected variable.

Figure 22 displays our three representative  $\delta$  Scuti variables. In the left panel is UCAC4-571-024831, with a period of 0.1741 days and an amplitude of 8 millimag. A *Gaia* DR2 match for this source measures  $T_{\text{eff}} \sim 5800$  K and  $L_* \sim 7.7 L_\odot$ . In the center panel is UCAC4-572-024661, with a period of 0.099 days and an amplitude of 0.009 mag. A *Gaia* DR2 match for this source measures  $T_{\text{eff}} \sim 5400$  K and  $L_* \sim 22 L_\odot$ . In the right panel is UCAC4-573-025256, with a period of 0.0584 days and an amplitude of 7 millimag. This variable is a new detection. A



### $\delta$ Scuti Variables

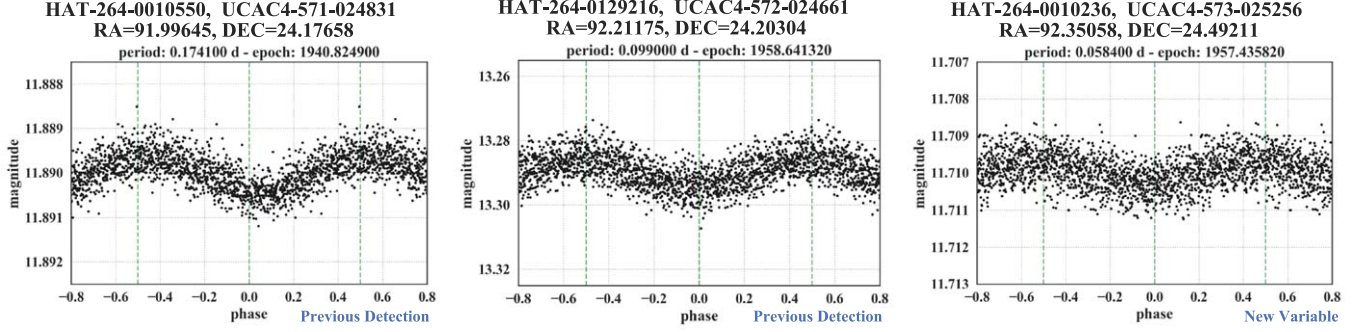


**Figure 22.** LCs of three representative  $\delta$  Scuti variables in our catalog. Plotted along the y-axis is the  $K_p$  magnitude. The first two columns display previously detected sources and the third column displays a new detection. *Left:* UCAC4-571-024831 with a period of 0.1741 days and an amplitude of 8 millimag. *Center:* UCAC4-572-024661 with a period of 0.099 days and an amplitude 0.009 mag. *Right:* UCAC4-573-025256 with a period of 0.0584 days and an amplitude of 7 millimag. UCAC4-573-025256 has an M35 membership probability of 60%, while the others are field sources.

### $\gamma$ Doradus Variables

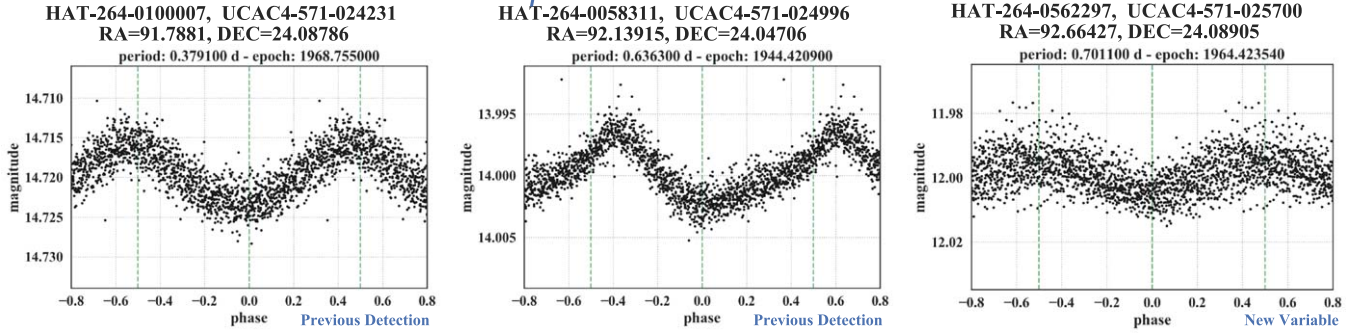


**Figure 23.** LCs of three representative  $\gamma$  Doradus variables in our catalog. Plotted along the y-axis is the  $K_p$  magnitude. The first two columns display previously detected sources and the third column displays a new detection. *Left:* UCAC4-571-024231, with a period of 0.3791 days and an amplitude of 8 millimag. *Center:* UCAC4-571-024996, with a period of 0.6363 days and an amplitude of 7 millimag. *Right:* UCAC4-571-025700, with a period of 0.7011 days and an amplitude of 0.01 mag. All sources are confirmed by *Gaia* to be field stars.

### Rotational Variables

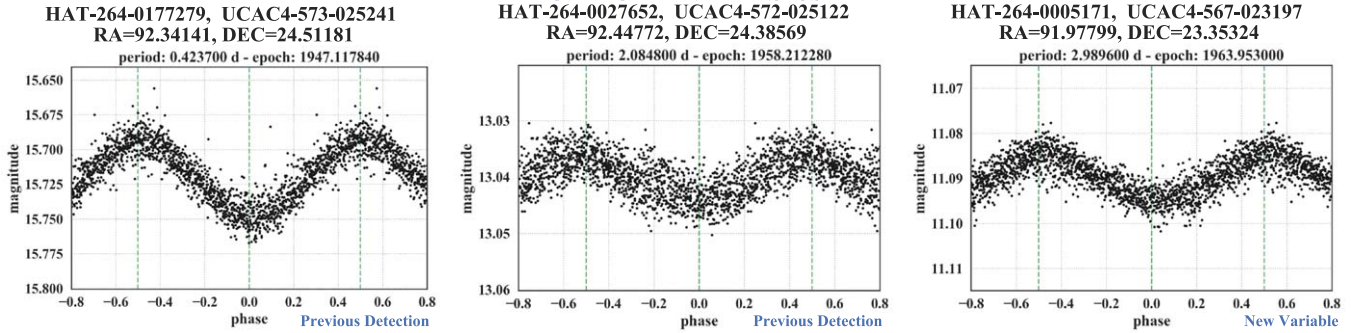


**Figure 24.** LCs of three representative rotational variables in our catalog. Plotted along the y-axis is the  $K_p$  magnitude. The first two columns display previously detected sources, and the third column displays a new detection. *Left:* UCAC4-573-025241, with a period of 0.4237 days and an amplitude of 0.06 mag. The *Gaia* DR2 match for this source measures  $T_{\text{eff}} \sim 4400$  K and  $L_* \sim 0.2 L_\odot$ . *Center:* UCAC4-572-025122, with a period of 2.0848 days and amplitude of 0.01 mag. The *Gaia* DR2 match for this source measures  $T_{\text{eff}} \sim 5370$  K and  $L_* \sim 2 L_\odot$ . *Right:* UCAC4-567-023197, with a period of 2.9896 days and an amplitude of 0.01 mag. The *Gaia* DR2 match for this source measures  $T_{\text{eff}} \sim 5900$  K and  $L_* \sim 2 L_\odot$ . The proper motion and parallax of UCAC4-572-025122 indicate M35 membership, while the other two are field sources.

*Gaia* DR2 match for this source measures  $T_{\text{eff}} \sim 7700$  K and  $L_* \sim 11 L_\odot$ . The first two panels are field sources, while the third panel has an M35 affiliated membership probability of  $P_m = 0.6$ .

Figure 23 displays our three representative  $\gamma$  Doradus variables. In the left panel is UCAC4-571-024231, with a period of 0.3791 days and an amplitude of 8 millimag. The *Gaia* DR2 match for this source measures  $T_{\text{eff}} \sim 5300$  K and  $L_* \sim 4 L_\odot$ . In the center panel is UCAC4-571-024996, with a period of 0.6363 days and an amplitude of 7 millimag. The

*Gaia* DR2 match for this source measures  $T_{\text{eff}} \sim 5200$  K and  $L_* \sim 2 L_\odot$ . In the right panel is UCAC4-571-025700, with a period of 0.7011 days and an amplitude of 0.01 mag. This variable is a new detection. The *Gaia* DR2 match for this source measures  $T_{\text{eff}} \sim 5800$  K and  $L_* \sim 4 L_\odot$ . All variables are likely field sources.

Figure 24 displays our three representative rotational variables. In the left panel is UCAC4-573-025241, with a period of 0.42366 days and an amplitude of 0.06 mag. The *Gaia*

**Table 5**  
A Truncated Version of the Periodic Variable Catalog Obtained from Sources in the K2 Campaign-0 Super Stamp

No.	1 HATID	2 UCACID	3 R.A.	4 Decl.	5 Kepmag	6 <i>P</i>	7 dmag	8 Class			
0	HAT-264-0001505	UCAC4-571-025584	92.58066	24.02087	9.91	2.1412	0.2808	Pulsating			
1	HAT-264-0246791	UCAC4-573-025534	92.52146	24.59545	15.84	0.0356	0.0012	Misc			
2	HAT-264-0060077	UCAC4-571-024903	92.06060	24.05245	13.92	0.1301	0.0109	Misc			
3	HAT-264-0133407	UCAC4-571-025201	92.28923	24.17921	15.20	0.0899	0.0058	Misc			
4	HAT-264-0038220	UCAC4-572-024259	91.93485	24.39266	13.86	0.2156	0.0007	Misc			
No.	9 Class_string	10 Blend	11 LSP1	12 LSFAP1	13 LSSNR1	14 LSP2	15 LSFAP2	16 LSSNR2	17 LSP3	18 LSFAP3	
0	Cepheid	0	2.1268	9.7e-256	1358.1	2.3649	2.3e-46	173.8	1.9441	1.1e-18	
1	Misc	0	0.1195	3.9e-12	60.1	0.1288	1.0e-08	45.1	3.2670	5.3e-02	
2	Misc	0	0.1301	6.6e-310	3045.6	0.1008	1.0e-138	997.1	0.1309	2.5e-22	
3	Misc	0	0.1420	9.3e-01	12.8	0.3375	1.0e+00	8.2	0.1197	1.0e+00	
4	Misc	0	0.2156	3.6e-11	36.4	0.9239	2.3e-07	25.4	0.6106	4.3e-05	
No.	19 LSSNR3	20 PDM1	21 PDM2	22 PDM3	23 BLSP1	24 BLS1TDur	25 BLS1TDepth	26 BLSP2	27 BLS2TDur		
0	0.0	2.1412	4.2824	0.0405	NaN	NaN	NaN	NaN	NaN		
1	0.0	0.0523	0.1916	0.3053	NaN	NaN	NaN	NaN	NaN		
2	0.0	0.1301	0.2602	0.3903	NaN	NaN	NaN	NaN	NaN		
3	0.0	0.0899	0.2695	0.5389	NaN	NaN	NaN	NaN	NaN		
4	0.0	3.0471	7.9224	0.1306	NaN	NaN	NaN	NaN	NaN		
No.	28 BLS2TDepth	29 BLSP3	30 BLS3TDur	31 BLS3TDepth	32 Jmag	33 errJ	34 Hmag	35 errH	36 Kmag	37 errK	38 Bmag
0	NaN	NaN	NaN	NaN	8.91	0.02	8.60	0.02	8.47	0.02	11.61
1	NaN	NaN	NaN	NaN	15.17	0.04	14.84	0.05	14.85	0.08	15.80
2	NaN	NaN	NaN	NaN	13.31	0.02	13.06	0.03	13.04	0.03	15.36
3	NaN	NaN	NaN	NaN	14.06	0.03	13.74	0.03	13.57	0.03	16.70
4	NaN	NaN	NaN	NaN	12.02	0.02	11.31	0.02	11.13	0.02	16.22
No.	39 Vmag	40 Imag	41 GaiaID	42 d1	43 d2	44 Teff	45 T1	46 T2	47 Rad	48 R1	49 R2
0	10.74	9.50	3425495186047291392	3495.3	4551.7	4897.6	4853.4	5007.5	39.7	38.0	40.5
1	14.81	15.56	3426302910482311168	2355.7	4260.8	5202.9	4731.7	5406.0	NaN	NaN	NaN
2	14.67	13.66	3426255562760045056	3114.3	4304.8	5269.0	4957.5	5454.0	NaN	NaN	NaN
3	16.04	14.72	3426263362420856320	3993.6	7541.5	4960.5	4879.0	5007.0	NaN	NaN	NaN
4	14.69	13.11	3426279992534733312	2697.6	3179.7	4092.8	3993.0	4249.0	9.0	8.4	9.4
No.	50 Lum	51 L1	52 L2	53 EBV	54 PMRA	55 PMDEC	56 PM35CG18	57 PM35CM09	58 PM35K13		
0	818.7	652.1	985.2	0.597	0.544	−1.398	NaN	0.0	9.8		
1	NaN	NaN	NaN	0.564	0.599	−0.629	NaN	0.0	74.1		
2	NaN	NaN	NaN	0.619	0.598	−2.093	NaN	12.0	29.6		
3	NaN	NaN	NaN	0.499	0.364	−2.107	NaN	14.0	78.8		
4	20.5	16.3	24.6	0.535	−1.827	-5.453	NaN	0.0	36.7		
No.	59 PM35K13b	60 PN2158CG18	61 PN2158D06	62 PN2158K13	63 PN2158K13b	64 PM35	65 PN2158				
0	0.0	NaN	NaN	NaN	NaN	0.0	0.0				
1	0.0	NaN	NaN	NaN	NaN	0.0	0.0				
2	0.3	NaN	NaN	NaN	23.1	0.0	8.6				
3	0.0	NaN	NaN	NaN	89.7	99.2	0.0				
4	0.0	NaN	NaN	NaN	56.8	100.0	4.9				
No.	66 Match1	67 Match2	68 Match3	69 Match4	70 Match5	71 Comment					
0	4710	442	NaN	NaN	V0371 Gem	VSX match with Delta Cepheid...					
1	NaN	NaN	NaN	NaN	NaN	Possibly multi-periodic					
2	6386	54	9	NaN	NaN	...					
3	13490	247	NaN	NaN	NaN	...					
4	NaN	NaN	NaN	NaN	NaN	Object is spinning too quickly...					

**Note.** A description of the column contents can be found below.

(This table is available in its entirety in machine-readable form.)

match for this source measures  $T_{\text{eff}} \sim 4300$  K and  $L_* \sim 0.2 L_{\odot}$ . UCAC4-572-025122 is shown in the center panel, with a period of 2.08484 days and an amplitude of 0.01 mag. This rotational variable is a member of the M35 cluster, as confirmed by *Gaia* DR2 proper motion measurements. The *Gaia* DR2 match for this source measures  $T_{\text{eff}} \sim 5370$  K and  $L_* \sim 2 L_{\odot}$ . Shown in the right panel is UCAC4-567-023197, a newly detected rotational variable with a period of 2.990 days and an amplitude of 0.01 mag. The *Gaia* DR2 match for this source measures  $T_{\text{eff}} \sim 5900$  K and  $L_* \sim 2 L_{\odot}$ . This rotational variable is a probable field star.

## 11. Summary and Conclusions

We present the results of a variability search conducted on stars in the K2CO super stamp. This analysis was performed on our publicly released image-subtracted LCs for 3960 sources. The source magnitudes range between  $9.7 \text{ mag} < V < 18.7 \text{ mag}$ . We searched for periodic signatures between 0.03 and 31 days. We detected and classified a total of 1143 periodic variables. Cluster membership was ascertained for our catalog sources. Our image subtraction analysis and variability search reveals periodic variables that remain undetected in crowded fields using other reduction methods. Therefore, we stress the need to employ specialized techniques such as image subtraction to fully exploit crowded stellar fields.

Within our catalog, 523 of the variables are new detections. While no new  $\delta$  Cepheid variables were found, our analysis revealed an overtone associated with the previously detected source V0371 Gem. Our catalog contains a total of two newly detected candidate transiting exoplanets, 44 EBs, and 1097 stellar variables (primarily rotating and pulsating sources). Of our 44 EBs, seven sources are new detections, including one probable M35 member and one probable NGC 2158 member. Among our variable catalog sources, we found 331 members of M35 and 56 members of NGC 2158. A truncated version of our digital table is shown in Table 5 of the Appendix. The flexible edition of our variable catalog is digitally hosted at <https://k2.hatsurveys.org/archive/>.

We thank J. Auman, J. Hoffman, C. Malecki, R. Mathieu, A. Mao, and J. Wallace for the insightful conversations related to this work. This material is based upon work supported by the National Science Foundation Graduate Research Fellowship Program under grant No. DGE-1656466. Any opinions, findings, conclusions, or recommendations expressed in this material are those of the authors and do not necessarily reflect the views of the National Science Foundation. The data in our analysis were provided by the K2 mission, funded by the NASA Science Mission directorate. Photometric data were downloaded from the Barbara A. Mikulski Archive for Space Telescopes (MAST). This publication makes use of data products from the Two Micron All Sky Survey, which is a joint project of the University of Massachusetts and the Infrared Processing and Analysis Center/California Institute of Technology, funded by the National Aeronautics and Space Administration and the National Science Foundation. This research has made use of NASA's Astrophysics Data System Bibliographic Services. For our cluster information, we have made extensive use of the WEBDA database, operated at the Department of Theoretical Physics and Astrophysics of the Masaryk University. This paper has made use of data from the European Space Agency (ESA) mission *Gaia* (<https://www.cosmos.esa.int/gaia>), processed by the *Gaia* Data Processing and

Analysis Consortium (DPAC, <https://www.cosmos.esa.int/web/gaia/dpac/consortium>). Funding for the DPAC has been provided by national institutions, in particular the institutions participating in the *Gaia* Multilateral Agreement. This research has made use of NASA's Astrophysics Data System Bibliographic Services. Lastly, we would like to acknowledge the VizieR catalog access tool, CDS, Strasbourg, France. The original description of the VizieR service was published in A&AS 143, 23.

*Facilities:* Kepler (K2), *Gaia*, MAST, ADS, Exoplanet Archive.

*Software:* Astrobase<sup>9</sup> (Bhatti et al. 2018), Astropy<sup>10</sup> (Astropy Collaboration et al. 2018), BATMAN (Kreidberg 2015), FITSH<sup>11</sup> (Pál 2012), Matplotlib (Hunter 2007), Numpy (van der Walt et al. 2011) Pandas (McKinney 2010), Scikit-learn (Pedregosa et al. 2011), VARTOOLS<sup>12</sup> (Hartman & Bakos 2016).

## Appendix

1. *HATID*—Source identifier as provided by the *Hungarian-made Automated Telescope Network*, also known as the *kepid* in the K2CO LC data set. If the HATID was unavailable, the source was identified solely using the UCAC source ID.
2. *UCACID*—Original source ID in UCAC catalog.
3. *R.A.*—Right ascension coordinate in degrees.
4. *Decl.*—Declination coordinate in degrees.
5. *Kepmag*—Kepler magnitude, as computed using 2MASS catalog values for sdssg and sdssr. Calculation follows the hierarchical scheme outlined in the Barbara A. Mikulski Archive for Space Telescopes (MAST).
6. *P*—The best determined period of the source (in days) from the periodogram analysis.
7. *dmag*—Amplitude of the magnitude (maximum peak value—minimum peak value) calculated after fitting an order-3 Fourier series to the differential magnitude time series.
8. *Class*—Variable classification identifier. Possible classification labels include *Transit*, *EB*, *Pulsating*, *Rotating*, and *Misc*.
9. *Class\_string*—Variable subclassification identifier. This identifier can provide additional information for rotating and pulsating variables. Possible subclassification labels include *Transit*, *EB*, *Cepheid*, *DScuti* ( $\delta$  Scuti pulsator), *GDor* ( $\gamma$  Doradus pulsator), *SPB* (slowly pulsating B-star), *RotVar* (rotational variable of indeterminate type), and *Misc* (indeterminate variable).
10. *Blend*—Boolean to indicate whether or not the source is an ambiguous blend. The value 0 indicates that the source is an identified primary variable, while the value 1 indicates that the source is an ambiguous blend.
11. *LSPI*—First peak period as determined by the LS periodogram (VARTOOLS).
12. *LSFAP1*—VARTOOLS-derived formal false alarm probability of the 1st peak period (VARTOOLS).
13. *LSSNRI*—S/N for the first peak period (VARTOOLS).

<sup>9</sup> <https://pypi.org/project/astrobase>

<sup>10</sup> <http://www.astropy.org>

<sup>11</sup> <https://fitsh.net>

<sup>12</sup> <https://www.astro.princeton.edu/~jhartman/vartools.html>



14. *LSP2*—Second peak period as determined by the LS periodogram (VARTOOLS).
15. *LSFAP2*—VARTOOLS-derived formal false alarm probability of the second peak period (VARTOOLS).
16. *LSSNR2*—S/N for the second peak period (VARTOOLS).
17. *LSP3*—Third peak period, as determined by the LS periodogram (VARTOOLS).
18. *LSFAP3*—VARTOOLS-derived formal false alarm probability of the third peak period (VARTOOLS).
19. *LSSNR3*—S/N for the third peak period (VARTOOLS).
20. *PDM1*—First peak period, as determined by the PDM periodogram (Astrobase).
21. *PDM2*—Second peak period, as determined by the PDM periodogram (Astrobase).
22. *PDM3*—Third peak period, as determined by the PDM periodogram (Astrobase).
23. *BLSP1*—First BLS peak period in days (Astrobase). Values are only listed for candidate EB and transit sources.
24. *BLS1TDur*—First BLS peak period transit duration in days (Astrobase).
25. *BLS1TDepth*—First BLS peak period transit depth, in mag (Astrobase).
26. *BLSP2*—Second BLS peak period, in days (Astrobase). Values are only listed for candidate EB and transit sources.
27. *BLS2TDur*—Second BLS peak period transit duration, in days (Astrobase).
28. *BLS2TDepth*—Second BLS peak period transit depth, in mag (Astrobase).
29. *BLSP3*—Third BLS peak period, in days (Astrobase).
30. *BLSTDdur*—Third BLS peak period transit duration, in days (Astrobase).
31. *BLS3TDepth*—Third BLS peak period transit depth, in mag (Astrobase). Values are only listed for candidate EB and transit sources.
32. *Jmag*—*J* band magnitude (UCAC4).
33. *errJ*—Error on the value of the *J* band magnitude (UCAC4).
34. *Hmag*—*H* band magnitude (UCAC4).
35. *errH*—Error on the value of the *H* band magnitude (UCAC4).
36. *Kmag*—*K* band magnitude (UCAC4).
37. *errK*—Error on the value of the *K* band magnitude (UCAC4).
38. *Bmag*—*B* band magnitude (UCAC4).
39. *Vmag*—*V* band magnitude (UCAC4).
40. *Imag*—*I* band magnitude (UCAC4).
41. *GaiaID*—Designated *Gaia* ID for source match.
42. *d1*—Minimum source distance, in parsecs, derived from the *Gaia* DR2 absolute stellar parallax at the reference epoch and the standard error of parallax.
43. *d2*—Maximum source distance, in parsecs, derived from the *Gaia* DR2 absolute stellar parallax at the reference epoch and the standard error of parallax.
44. *Teff*—*Gaia* DR2 estimate of stellar effective temperature (in Kelvin) from Apsis-Priam.
45. *T1*—*Gaia* DR2 uncertainty (lower) on *Teff* estimate from Apsis-Priam. This is the 16th percentile of the probability distribution function over *Teff*.
46. *T2*—*Gaia* DR2 uncertainty (upper) on *Teff* estimate from Apsis-Priam. This is the 84th percentile of the probability distribution function over *Teff*.
47. *Rad*—*Gaia* DR2 stellar radius estimate from Apsis-Priam. Listed in units of solar radii.
48. *R1*—*Gaia* DR2 uncertainty (lower) on radius estimate from Apsis-FLAME. This is the 16th percentile of the probability distribution function over radius. Listed in units of solar radii.
49. *R2*—*Gaia* DR2 uncertainty (upper) on radius estimate from Apsis-FLAME. This is the 84th percentile of the probability distribution function over radius. Listed in units of solar radii.
50. *Lum*—*Gaia* DR2 estimate of luminosity from Apsis-FLAME. Listed in units of solar luminosity.
51. *L1*—*Gaia* DR2 uncertainty (lower) on luminosity estimate from Apsis-FLAME. This is the 16th percentile of the probability distribution function over luminosity. Listed in units of solar luminosity.
52. *L2*—*Gaia* DR2 uncertainty (upper) on luminosity estimate from Apsis-FLAME. This is the 84th percentile of the probability distribution function over luminosity. Listed in units of solar luminosity.
53. *E(B−V)*—*E(B−V)* extinction as provided by Schlafly & Finkbeiner (2011).
54. *PMRA*—Proper motion in R.A. ( $\text{mas yr}^{-1}$ ) from *Gaia* DR2.
55. *PMDEC*—Proper motion in decl. ( $\text{mas yr}^{-1}$ ) from *Gaia* DR2.
56. *PM35CG18*—M35 membership probability from *Gaia* (Cantat-Gaudin et al. 2018).
57. *PM35CM09*—M35 membership probability, determined with proper motion measurements (Bouy et al. 2015).
58. *PM35K13*—M35 membership probability, determined with proper motion measurements (Kharchenko et al. 2013).
59. *PM35K13b*—M35 membership probability from CMD (Kharchenko et al. 2013).
60. *PN2158CG18*—Membership probability for affiliation with NGC 2158 from *Gaia* (Cantat-Gaudin et al. 2018). Oddly, some of these probabilities were reported as 100%.
61. *PN2158D06*—NGC 2158 membership probability, determined with proper motion measurements (Dias et al. 2006).
62. *PN2158K13*—NGC 2158 membership probability, determined with proper motion measurements (Kharchenko et al. 2013).
63. *PN2158K13b*—NGC 2158 membership probability from CMD (Kharchenko et al. 2013).
64. *PM35*—the overall designated M35 membership probability used for the source, employing the method described in Section 3.4.
65. *PN2158*—the overall designated NGC 2158 membership probability used for the source, employing the method described in Section 3.4, which includes a King model fit to weight cluster membership according to the radial distance from the cluster core.
66. *Match1*—Corresponding source catalog match from the variable catalog presented in Libralato et al. (2016).

67. *Match2*—Corresponding source catalog match from the variable catalog presented in Nardiello et al. (2015).
68. *Match3*—Corresponding source catalog match from the variable catalog presented in Meibom et al. (2009).
69. *Match4*—Corresponding source catalog match from the variable catalog presented in Mochejska et al. (2004).
70. *Match5*—Corresponding source catalog match from the VSX Catalog.
71. *Comment*—Source commentary.

### ORCID iDs

M. Soares-Furtado  <https://orcid.org/0000-0001-7493-7419>  
 J. D. Hartman  <https://orcid.org/0000-0001-8732-6166>  
 W. Bhatti  <https://orcid.org/0000-0002-0628-0088>  
 L. G. Bouma  <https://orcid.org/0000-0002-0514-5538>  
 T. Barna  <https://orcid.org/0000-0002-4843-345X>  
 G. Á. Bakos  <https://orcid.org/0000-0001-7204-6727>

### References

- Adams, F. C., & Laughlin, G. 2006, *ApJ*, **649**, 1004  
 Alard, C. 2000, *A&AS*, **144**, 363  
 Alard, C., & Lupton, R. H. 1998, *ApJ*, **503**, 325  
 Angus, R., Aigrain, S., Foreman-Mackey, D., & McQuillan, A. 2015, *MNRAS*, **450**, 1787  
 Astropy Collaboration, Price-Whelan, A. M., Sipőcz, B. M., et al. 2018, *AJ*, **156**, 123  
 Barnes, S. A. 2003, *ApJ*, **586**, 464  
 Barnes, S. A. 2007, *ApJ*, **669**, 1167  
 Barnes, S. A. 2010, *ApJ*, **722**, 222  
 Barrado y Navascués, D., Deliyannis, C. P., & Stauffer, J. R. 2001, *ApJ*, **549**, 452  
 Bhatti, W., Bouma, L., Wallace, J., & Price-Whelan, A. 2018, Waqasbhatti/Astrobase: Astrobase v0.3.14, Zenodo, doi:10.5281/zenodo.1246769  
 Bouy, H., Bertin, E., Barrado, D., et al. 2015, *A&A*, **575**, A120  
 Brewer, L. N., Sandquist, E. L., Mathieu, R. D., et al. 2016, *AJ*, **151**, 66  
 Buchler, J. R. 2008, *ApJ*, **680**, 1412  
 Buchler, J. R., & Szabó, R. 2007, *ApJ*, **660**, 723  
 Cantat-Gaudin, T., Jordi, C., Vallenari, A., et al. 2018, *A&A*, **618**, 93  
 Carraro, G., Girardi, L., & Marigo, P. 2002, *MNRAS*, **332**, 705  
 Ciardi, D. R., Crossfield, I. J. M., Feinstein, A. D., et al. 2018, *AJ*, **155**, 10  
 Cudworth, K. M. 1971, *AJ*, **76**, 475  
 Curtis, J. L., Wolfgang, A., Wright, J. T., Brewer, J. M., & Johnson, J. A. 2013, *AJ*, **145**, 134  
 David, T. J. 2018, PhD thesis, California Inst. Tech.  
 Dias, W. S., Assafin, M., Flório, V., Alessi, B. S., & Líbero, V. 2006, *A&A*, **446**, 949  
 Dias, W. S., Lépine, J. R. D., & Alessi, B. S. 2001, *A&A*, **376**, 441  
 Epstein, C. R., & Pinsonneault, M. H. 2014, *ApJ*, **780**, 159  
 Gallet, F., & Bouvier, J. 2013, *A&A*, **556**, A36  
 Girardi, L., Bressan, A., Bertelli, G., & Chiosi, C. 2000, *A&AS*, **141**, 371  
 Hartman, J. D., & Bakos, G. Á. 2016, *A&C*, **17**, 1  
 Hartman, J. D., Bakos, G. Á., Kovács, G., & Noyes, R. W. 2010, *MNRAS*, **408**, 475  
 Hartman, J. D., Gaudi, B. S., Pinsonneault, M. H., et al. 2009, *ApJ*, **691**, 342  
 Huang, C. X., Penev, K., Hartman, J. D., et al. 2015, *MNRAS*, **454**, 4159  
 Hunter, J. D. 2007, *CSE*, **9**, 90  
 Irwin, J., & Bouvier, J. 2009, in Proc. IAU Symp. 258, The Age of Stars, ed. E. E. Mamajek, D. R. Soderblom, & R. F. G. Wyse (Cambridge: Cambridge Univ. Press), 363  
 Irwin, J., Hodgkin, S., Aigrain, S., et al. 2008, *MNRAS*, **383**, 1588  
 Jacobson, H. R., Friel, E. D., & Pilachowski, C. A. 2009, *AJ*, **137**, 4753  
 Jordi, C., Gebran, M., Carrasco, J. M., et al. 2010, *A&A*, **523**, A48  
 Kalirai, J. S., Fahlman, G. G., Richer, H. B., & Ventura, P. 2003, *AJ*, **126**, 1402  
 Karttunen, H., Kröger, P., Oja, H., Poutanen, M., & Donner, K. J. 2017, *Fundamental Astronomy* (Berlin: Springer)  
 Kawaler, S. D. 1989, *ApJL*, **343**, L65  
 Kharchenko, N. V., Piskunov, A. E., Schilbach, E., Röser, S., & Scholz, R.-D. 2013, *A&A*, **558**, A53  
 King, I. 1962, *AJ*, **67**, 471  
 Kovács, G., Bakos, G., & Noyes, R. W. 2005, *MNRAS*, **356**, 557  
 Kovács, G., Zucker, S., & Mazeh, T. 2002, *A&A*, **391**, 369  
 Kreidberg, L. 2015, *PASP*, **127**, 1161  
 LaCourse, D. M., Jek, K. J., Jacobs, T. L., et al. 2015, *MNRAS*, **452**, 3561  
 Libralato, M., Bedin, L. R., Nardiello, D., & Piotto, G. 2016, *MNRAS*, **456**, 1137  
 Li, C., Deng, L., de Grijs, R., Jiang, D., & Xin, Y. 2018, *ApJ*, **856**, 25  
 Mamajek, E. E., & Hillenbrand, L. A. 2008, *ApJ*, **687**, 1264  
 Mandel, K., & Agol, E. 2002, *ApJL*, **580**, L171  
 McKinney, W. 2010, in Proc. 9th Python in Science Conf., ed. S. van der Walt & J. Millman (Austin, TX: SciPy), 51  
 Meibom, S., Barnes, S. A., Latham, D. W., et al. 2011, *ApJL*, **733**, L9  
 Meibom, S., Barnes, S. A., Platais, I., et al. 2015, *Natur*, **517**, 589  
 Meibom, S., Mathieu, R. D., & Stassun, K. G. 2009, *ApJ*, **695**, 679  
 Meibom, S., Torres, G., Fressin, F., et al. 2013, *Natur*, **499**, 55  
 Mochejska, B. J., Stanek, K. Z., Sasselov, D. D., et al. 2004, *AJ*, **128**, 312  
 Mochejska, B. J., Stanek, K. Z., Sasselov, D. D., et al. 2006, *AJ*, **131**, 1090  
 Molnár, L., Plachy, E., Juhász, Á. L., & Rimoldini, L. 2018, *A&A*, **620**, A127  
 Nardiello, D., Bedin, L. R., Nascimbeni, V., et al. 2015, *MNRAS*, **447**, 3536  
 Pál, A. 2012, *MNRAS*, **421**, 1825  
 Pedregosa, F., Varoquaux, G., Gramfort, A., et al. 2011, *J. Mach. Learn. Res.*, **12**, 2825  
 Pont, F., Zucker, S., & Queloz, D. 2006, *MNRAS*, **373**, 231  
 Portegies Zwart, S. F., McMillan, S. L. W., & Gieles, M. 2010, *ARA&A*, **48**, 431  
 Reiners, A., & Mohanty, S. 2012, *ApJ*, **746**, 43  
 Roeser, S., Demleitner, M., & Schilbach, E. 2010, *AJ*, **139**, 2440  
 Sanders, W. L. 1971, *A&A*, **14**, 226  
 Sandquist, E. L., Mathieu, R. D., Brogaard, K., et al. 2013, *ApJ*, **762**, 58  
 Sarro, L. M., Bouy, H., Bertin, E., et al. 2014, *yCat*, **563**, A45  
 Scargle, J. D. 1982, *ApJ*, **263**, 835  
 Schlafly, E. F., & Finkbeiner, D. P. 2011, *ApJ*, **737**, 103  
 Shapley, H. 1930, *HarMo*, **2**  
 Skumanich, A. 1972, *ApJ*, **171**, 565  
 Smolec, R., & Moskalik, P. 2010, *A&A*, **524**, A40  
 Soares-Furtado, M., Hartman, J. D., Bakos, G. Á., et al. 2017, *PASP*, **129**, 044501  
 Stellingwerf, R. F. 1978, *ApJ*, **224**, 953  
 Sung, H., & Bessell, M. S. 1999, *MNRAS*, **306**, 361  
 Vanderburg, A., & Johnson, J. A. 2014, *PASP*, **126**, 948  
 van der Walt, S., Colbert, S. C., & Varoquaux, G. 2011, *CSE*, **13**, 22  
 Vidal, N. V. 1973, *A&AS*, **11**, 93  
 Wallace, J. J., Hartman, J. D., Bakos, G. Á., & Bhatti, W. 2019a, *ApJS*, **244**, 12  
 Wallace, J. J., Hartman, J. D., Bakos, G. Á., & Bhatti, W. 2019b, *ApJL*, **870**, L7  
 Watson, C., Henden, A. A., & Price, A. 2017, *yCat*, **102027**  
 Watson, C. L., Henden, A. A., & Price, A. 2006, *SASS*, **25**, 47  
 Weber, E. J., & Davis, L., Jr. 1967, *ApJ*, **148**, 217  
 Williams, K. A., Bolte, M., & Koester, D. 2009, *ApJ*, **693**, 355  
 Yi, S., Demarque, P., Kim, Y.-C., et al. 2001, *ApJS*, **136**, 417  
 Zechmeister, M., & Kürster, M. 2009, *A&A*, **496**, 577  
 Zhu, W., Huang, C. X., Udalski, A., et al. 2017a, *PASP*, **129**, 104501  
 Zhu, W., Udalski, A., Huang, C. X., et al. 2017b, *ApJL*, **849**, L31